nature materials

SUPPLEMENTARY INFORMATION

DOI: 10.1038/NMAT4759

Quasicrystalline nanocrystal superlattice with partial matching rules

Xingchen Ye[1,†], Jun Chen[1,2†], M. Eric Irrgang[3,4,†], Michael Engel[4,5,†], Angang Dong[6], Sharon C. Glotzer[3,4,5,*], Christopher B. Murray[1,2,*]

[1]Department of Chemistry, [2]Department of Materials Science and Engineering, University of Pennsylvania, Philadelphia, Pennsylvania 19104, USA.

[3]Department of Materials Science and Engineering, [4]Biointerfaces Institute, [5]Department of Chemical Engineering, University of Michigan, Ann Arbor, Michigan 48109, USA.

[6]Department of Chemistry and Collaborative Innovation Center of Chemistry for Energy Materials, Fudan University, Shanghai 200433, China.

†These authors contributed equally.

*Corresponding authors: sglotzer@umich.edu, cbmurray@sas.upenn.edu

DOI: 10.1038/NMAT4759

Supplementary Discussion

1. Quasicrystal tiling analysis

Four-dimensional vertex coordinates. The matrix

$$\mathbf{P} = \begin{pmatrix} \mathbf{P}^{\parallel} \\ \mathbf{P}^{\perp} \end{pmatrix} = \begin{pmatrix} 1 & \sqrt{3}/2 & 1/2 & 0 \\ 0 & 1/2 & \sqrt{3}/2 & 1 \\ \hline 1 & -\sqrt{3}/2 & 1/2 & 0 \\ 0 & 1/2 & -\sqrt{3}/2 & 1 \end{pmatrix} a$$

projects $\boldsymbol{x}_i{}^{(4)}$ on the two-dimensional (ideal) vertex position $\boldsymbol{x}_i{}^{\parallel} = \mathbf{P}^{\parallel}\boldsymbol{x}_i{}^{(4)}$ in physical (parallel) space, describing the ideal, i.e. phonon strain-corrected position of the vertex, and on the two-dimensional position $\boldsymbol{x}_i{}^{\perp} = \mathbf{P}^{\perp}\boldsymbol{x}_i{}^{(4)}$ in internal (perpendicular) space, quantifying the amount of phason displacement, i.e. the deviation from ideal quasiperiodic order (Supplementary Fig. 18,19).

Occupation domain and comparison to ideal tiling. Analyzing the distribution of distances in perpendicular space, $\boldsymbol{x}_i{}^{\perp} - \boldsymbol{x}_0{}^{\perp}$, allowed assessing the tiling quality and distinguishes quasicrystals and approximants. The distribution is compact and called the occupation domain. In agreement with DDQCs found in alloys, occupation domains were thermally broadened (Supplementary Fig. 20). Anisotropic faceting or fractal shape, which occurs in occupation domains of square-triangle tilings generated by inflation schemes (Supplementary Fig. 21), was not present.

Presence of dislocations. The starting point of the network exploration and the presence of dislocations affected the lifting procedure (Supplementary Fig. 22). Each dislocation caused a string of detected coordinates to disagree by a Burgers vector $\boldsymbol{b}$ (Supplementary Figs. 23-25), which is a four-dimensional vector that projects on a small vector in parallel space $\boldsymbol{b}^{\parallel} = \mathbf{P}^{\parallel}\boldsymbol{b}$ (phonon component) and a larger vector in perpendicular space $\boldsymbol{b}^{\perp} = \mathbf{P}^{\perp}\boldsymbol{b}$ (phason component). We analyzed the frequency of disagreements (lifting continuity violations) in three TEM samples. In Supplementary Table 1, Burgers vectors are grouped by symmetry equivalence. Most frequently found is the Burgers vector type $(0,1,-2,1)$, which corresponds to the smallest phonon component in our samples.

Phason displacement analysis. The relationship $r^{\perp}(r^{\parallel}) = \left\langle r_{ij}{}^{\perp} \middle| r_{ij}{}^{\parallel} \approx r^{\parallel} \right\rangle_{ij}$ between the parallel space distance $r_{ij}{}^{\parallel} = \left\|\mathbf{P}^{\parallel}(\boldsymbol{x}_i{}^{(4)} - \boldsymbol{x}_j{}^{(4)})\right\|$ and the perpendicular space distance $r_{ij}{}^{\perp} = \left\|\mathbf{P}^{\perp}(\boldsymbol{x}_i{}^{(4)} - \boldsymbol{x}_j{}^{(4)})\right\|$, obtained by averaging over pairs (i,j), is called phason displacement. Lower values correspond to a more compact occupation domain. At longer distances, phason displacement increases. Because dislocations create discontinuities, we limited the analysis to regions not including any dislocations. Such regions have at most a few thousand points. Although the growth of phason displacement with $r^{\parallel}$ depends on the starting point of tile vertex detection, the general shape of the curve remained unchanged (Supplementary Fig. 26). We therefore chose the centermost input point as the starting vertex in Fig. 3.

2. Packing of hard particles

We tested whether the appearance of the DDQC or the σ-phase can be understood from consideration of particle shape alone. In particular we are interested in whether either phase can be competitive with phase separation of the sample into close-packed crystals of the two particle species individually. We conjecture that the relative packing density of the DDQC and the σ-phase is representative of their relative stability at high density.

The large (L) and small (S) metallic nanoparticles used in this study have shapes somewhat between spheres and truncated octahedra (Supplementary Figs. 1-2). Systems were parameterized in two different ways and parameter space was swept to optimize a candidate for dense packing. In the *first parameterization*, small particles were assumed to be spherical enough to be considered as such, while the larger particles were sphero-truncated octahedra. Parameters are the ratio of the circumradii of the two particles and the ratio of the rounding radius to the overall circumradius of the larger particle. The *second parameterization* assumed that rounding radii are determined primarily by the oleic acid ligand coating, which is further assumed to be identical on both particles. Large and small particles are sphero-truncated octahedra with the same rounding radius. Adjustable parameters are the ratio of circumradii of the two particles and the ratio of the rounding radius to the overall circumradius of the smaller particle.

We used the σ-phase unit cell as a starting configuration and searched in the neighborhood of the candidate structure. As a baseline we considered the densest packing of sphero-truncated octahedra (Supplementary Fig. 27) and calculated the packing fraction η when the two particle species phase separate,

$$\eta = \frac{1 + N_r V_r}{1 + N_r V_r \eta_L / \eta_S} \eta_L,$$

where $N_r = N_S/N_L = 7.5$ is the stoichiometry (small-to-large) of the σ-phase, the volume ratio $V_r = V_S/V_L$ in terms of the circumsphere R and the size radio, and the single-species packing fractions η_L and η_S are taken from Supplementary Fig. 27. We find that although density can be readily improved over binary sphere packing, the density of the σ-phase is always lower than phase-separated dense packing (Supplementary Fig. 28). This indicates that a hard particle model alone cannot explain the σ-phase or the quasicrystal.

Nevertheless, the hard particle compressions demonstrate that the sphero-truncated octahedra have preferred orientations. A two-fold axis of the polyhedra aligns with the 12-fold axis of the tiling. Although the clusters of large particles give the impression of the Voronoi cells of four neighboring particles in a BCC lattice, the orientation compatible with BCC is not strongly favored. Contacts occur preferentially between like faces. Deviation from BCC local neighborhoods may be necessary for long-range order due to constraints on the angles between neighboring particles.

3. Molecular dynamics simulations

We test the feasibility of stabilizing or self-assembling the observed DDQC using a coarse-grained model of NCs with an interaction ansatz for metallic nanoparticles with an oleic acid ligand coating. For hard particle simulations, the best packing sphero-truncated octahedra had a circumsphere ratio of $r_S/r_L = 0.625$ and rounding radius $R/r_S = 0.3$ (Supplementary Fig. 28). We

DOI: 10.1038/NMAT4759

assume (per the experiments) that the metallic core of the smaller particles has circumsphere diameter $d_S = 6.8$ nm, which gives $r_S = d_S/2/(1 - R/r_S) = 4.86$ nm. The ligand coating thickness is then $R = 1.46$ nm and the larger particle metallic core has circumsphere diameter $d_L = 2(r_L - R) = 12.6$ nm. For the small particles, then, we choose $r_0 = 9.7$, on which the other length scales are based.

We introduced an attractive Morse potential, $\phi(r) = D(e^{-2\alpha(r-r_0)} - 2\,e^{-\alpha(r-r_0)})$ to represent an orientationally averaged interparticle interaction. We bias against demixing by using hetero-attraction (small-large pairs) only. The Morse parameters r_0, D, α allow us to tune the location, strength, and width of the attractive well. The repulsive part of the potential between like particles was mapped to a shifted and truncated Morse potential

$$\phi(r) = \begin{cases} D\left(e^{-2\alpha(r-r_0)} - 2\,e^{-\alpha(r-r_0)}\right) + D & \text{for } 0 \le r \le r_0, \\ 0 & \text{for } r_0 \le r. \end{cases}$$

We scanned parameters around the 0.625 size ratio, which gives competitive packing (Supplementary Fig. 28), to find the potential width, depth (strength), and range (size ratio) that best stabilized a constructed σ-phase. Size ratio is determined by the cut-off radius r_{cut}, which is averaged to define the center of the attractive well in the L–S interaction. For a size ratio of 0.556, we used Morse potential parameters $r_0 = 9.7, 13.58, 17.46$ for S–S, S–L, and L–L particle pairs, respectively. For like particles we chose $r_{\text{cut}} = r_0$. For the S–L interaction we chose $r_{\text{cut}} = 2r_0$, and the potential and force were smoothed to zero beyond $0.9r_{\text{cut}}$. The truncation and smoothing causes a small offset of the potential minimum of about 5% of D. We performed simulations with interaction strength $3\,k_{\text{B}}T \le D \le 6\,k_{\text{B}}T$, for which $D = 5\,k_{\text{B}}T$ yielded the best assembly behavior (Figs. 4c-e in the main text). Interaction width is set by $\alpha = 0.3, 0.214, 0.167$ for the different types of particle pairs. The relationship between α for each pair type is determined by the ratio of r_0 of the larger to smaller particle to maintain similar potential shape for each particle type pair. Masses were assigned based on the ratio of presumed metallic core volumes.

Simulations were initialized using a seeded fluid with composition equal to the known quasicrystal tile ratio

$$\frac{N_S}{N_L} = \frac{16\sqrt{3} + 7 \cdot 4}{2\sqrt{3} + 4} = 4 + 2\sqrt{3} = 7.464\ldots$$

A target density was based on the density of stable, spherical seeds with open boundary conditions and later adjusted to apply a small amount of positive pressure on the seeded system. A simulation box of 17,000 particles was initialized at about half of the target density, then thermalized and compressed for 10^5 steps. Particles were removed from the resulting configuration to make room for a σ-phase seed, six unit cells in diameter containing 4459 particles. Configurations with the seed in place ranged from 18190 to 18249 particles. The seeded fluid was first relaxed with FIRE energy minimization in HOOMD and then brought to the target temperature through 10^4 steps of Langevin dynamics integration. Simulations were run for a total of up to $2 \cdot 10^9$ steps.

A few parameters were found for which the σ-phase grows. Seeded growth appears more rapid along the 12-fold axis and the seed grows to span the box in this direction early on. The crystal takes longer to begin to span the box in the perpendicular plane, though large particles can be seen to be forming layers very early on. Our simulation results establish that the width of the at-

tractive well and the particle size ratio are important factors in stabilizing the σ-phase or quasicrystal structure over competing phases. The best size and well width parameters for seeded growth are consistent with experimentally observed particle size ratio and surface variation.

4. Fourier transforms

We rationalize the Fourier transforms in Fig. 2. Because the T and P/P′ layers are close together, the particles in these layers also appear together in the slices extracted from the electron tomography reconstruction. This is clearly visible in the top row of Fig. 2a-e. For example, the slice for the T layer shows not only the open lattice indicated in the middle row, but also additional small nanocrystals from below and above. In the same way, the slices for the layers P and P′ include particles from the T layer, and as a result have a close resemblance to densely packed hexagonal layers. This explains why the bottoms of Fig. 2b,c are similar to the Fourier transform of a hexagonal lattice with only minor deviations (modulations of the hexagonal lattice) causing additional weak peaks.

Since the slice of layer T essentially combines features of both neighboring layers (P and P′), its Fourier transform is a superposition of the Fourier transform of the P layer and the Fourier transform of the P′ layer. For the slices of the M/M′ layer the situation is different. Here the description of the structure requires two clearly distinguished incommensurate length scales. The results are the more complicated patterns with well-defined peaks at longer wavelengths (bottom row of Fig. 2a,e).

5. Square-triangle tilings

There are only four possible vertex configurations in square-triangle tilings: 3^6 (six triangles), 4^4 (four squares), $3^3.4^2$ (three triangles neighboring a pair of squares), and $3^2.4.3.4$ (σ-phase). This list demonstrates that neither adjacent squares nor adjacent triangles can be avoided in any square-triangle tiling. Furthermore, this list shows that the fewest adjacent tiles of the same type (namely, one at each vertex) are found in the σ-phase. In comparison, the DDQC adds $3^3.4^2$ and 3^6 vertices, which increases the number of adjacent squares as well the number of adjacent triangles.

Burgers vector (type)	Phonon component	Phason component	Number detected
$(0,1,-2,1)$	**0.268**	3.73	**58**
$(2,-3,1,1)$	0.379	5.28	4
$(0,0,-1,1)$	0.518	**1.93**	**12**
$(0,1,-2,1)$	0.78	4.63	2

Supplementary Table 1. Number of lifting continuity violations in three $CoFe_2O_4$-Fe_3O_4 samples. Dislocations with small phonon component or small phason component occur most frequently (bold red).

DOI: 10.1038/NMAT4759

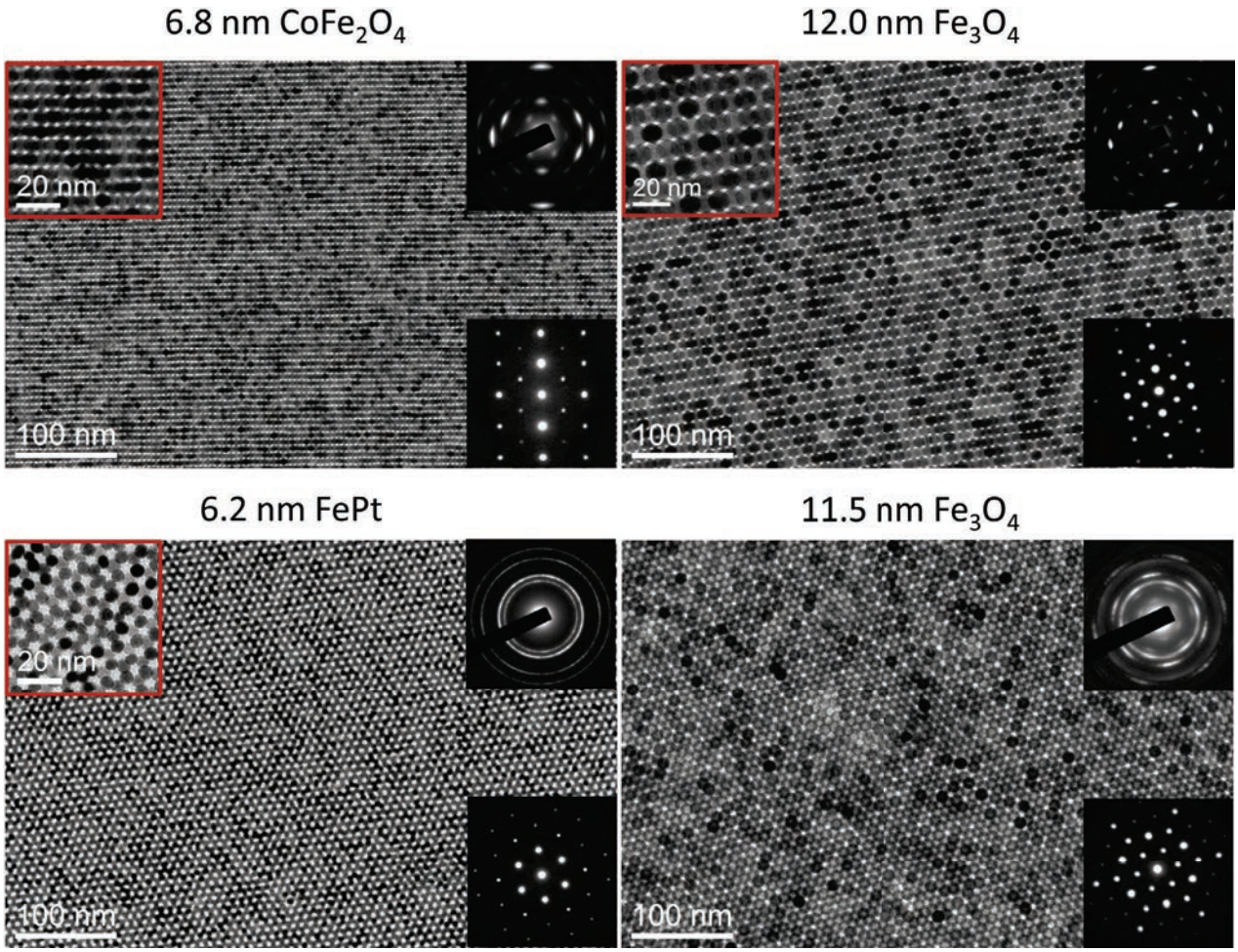

Supplementary Figure 1. Low-magnification and high-magnification (upper-left inset) TEM images of NCs used for the self-assembly of quasicrystalline BNSLs and corresponding WAED (upper-right inset) and SAED (lower-right inset) patterns. The combination of 6.8 nm $CoFe_2O_4$ and 12.0 nm Fe_3O_4 or 6.2 nm FePt and 11.5 nm Fe_3O_4 leads to quasicrystalline BNSL formation.

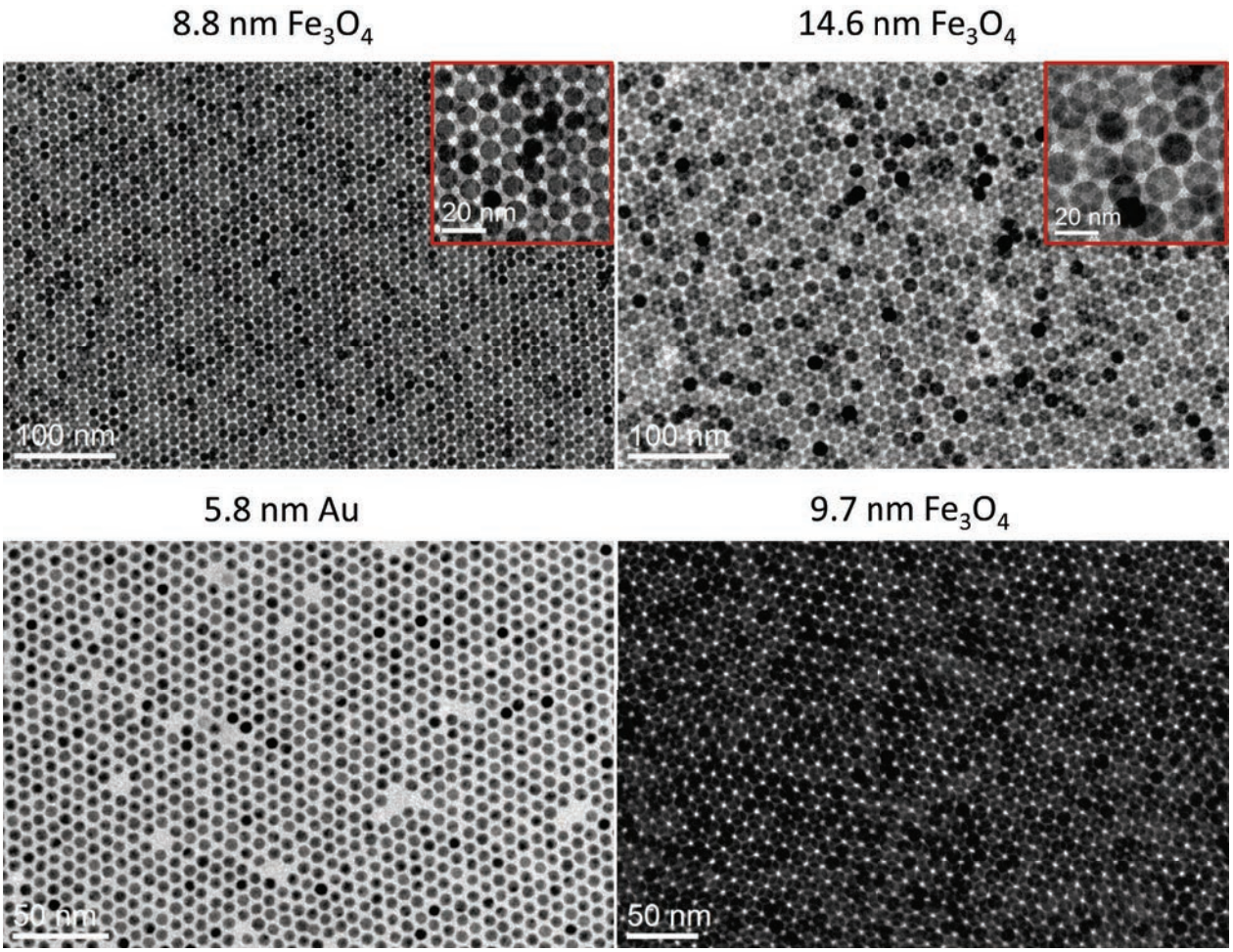

Supplementary Figure 2. Low-magnification and high-magnification (upper-right inset) TEM images of NCs used for the self-assembly of quasicrystalline BNSLs. The combination of 8.8 nm Fe_3O_4 and 14.6 nm Fe_3O_4 or 5.8 nm Au and 9.7 nm Fe_3O_4 leads to quasicrystalline BNSL formation.

DOI: 10.1038/NMAT4759

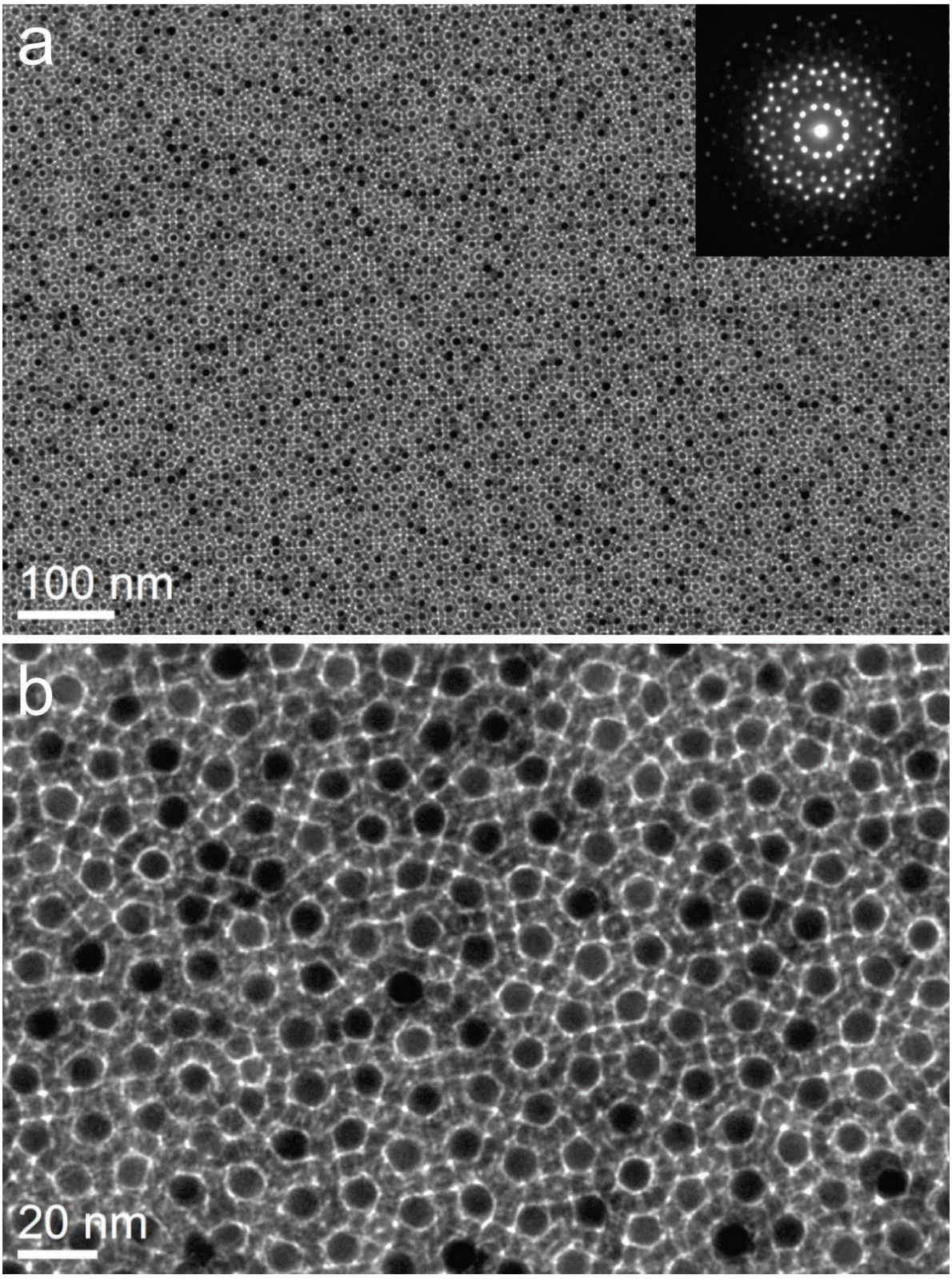

Supplementary Figure 3. (a) Low-magnification and corresponding SAED pattern (inset) and (b) high-magnification TEM images of DDQCs self-assembled from 6.8 nm $CoFe_2O_4$ and 12.0 nm Fe_3O_4 NCs.

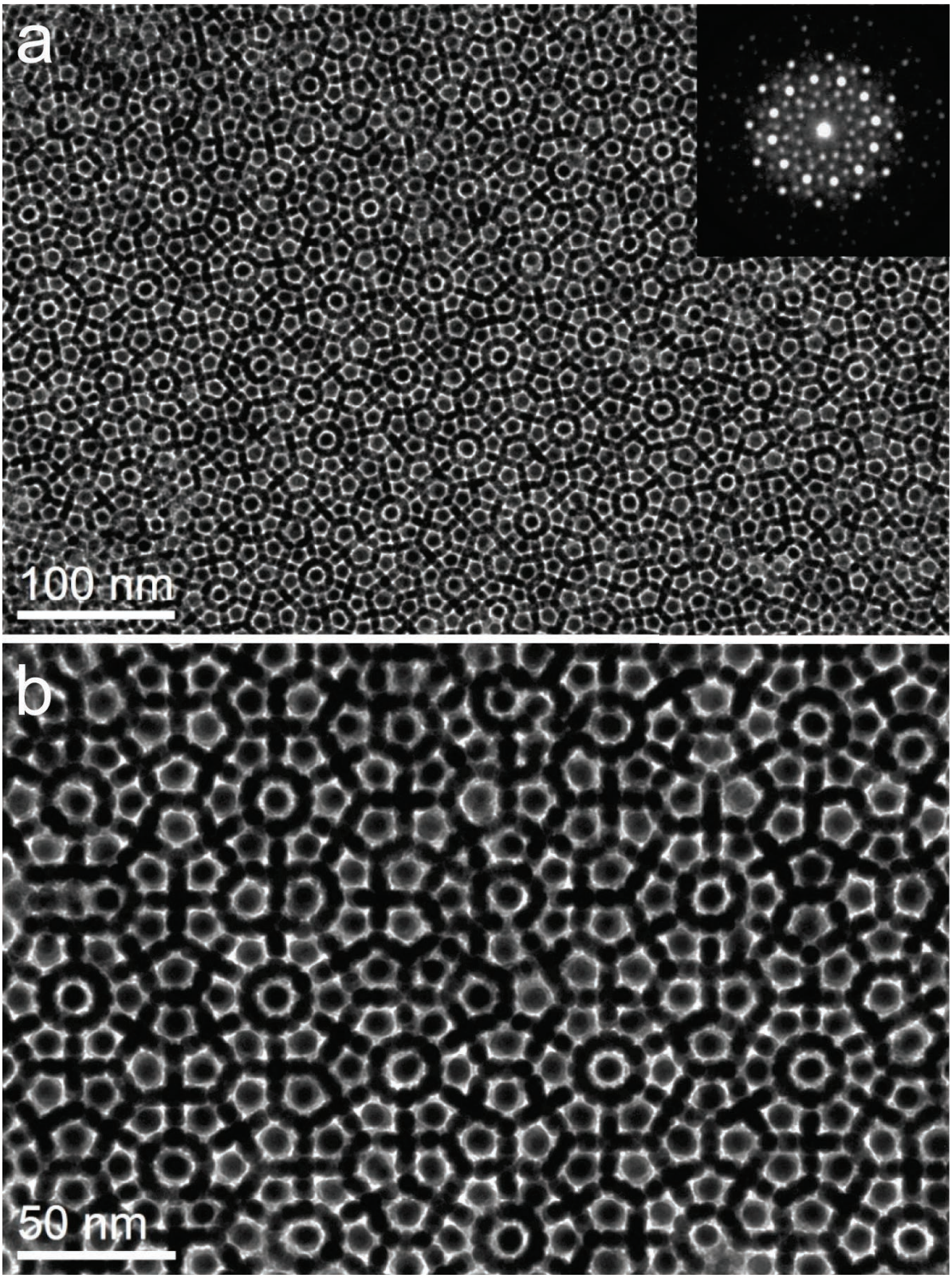

Supplementary Figure 4. (a) Low-magnification and corresponding SAED pattern (inset) and (b) high-magnification TEM images of DDQCs self-assembled from 6.2 nm FePt and 11.5 nm Fe_3O_4 NCs.

DOI: 10.1038/NMAT4759

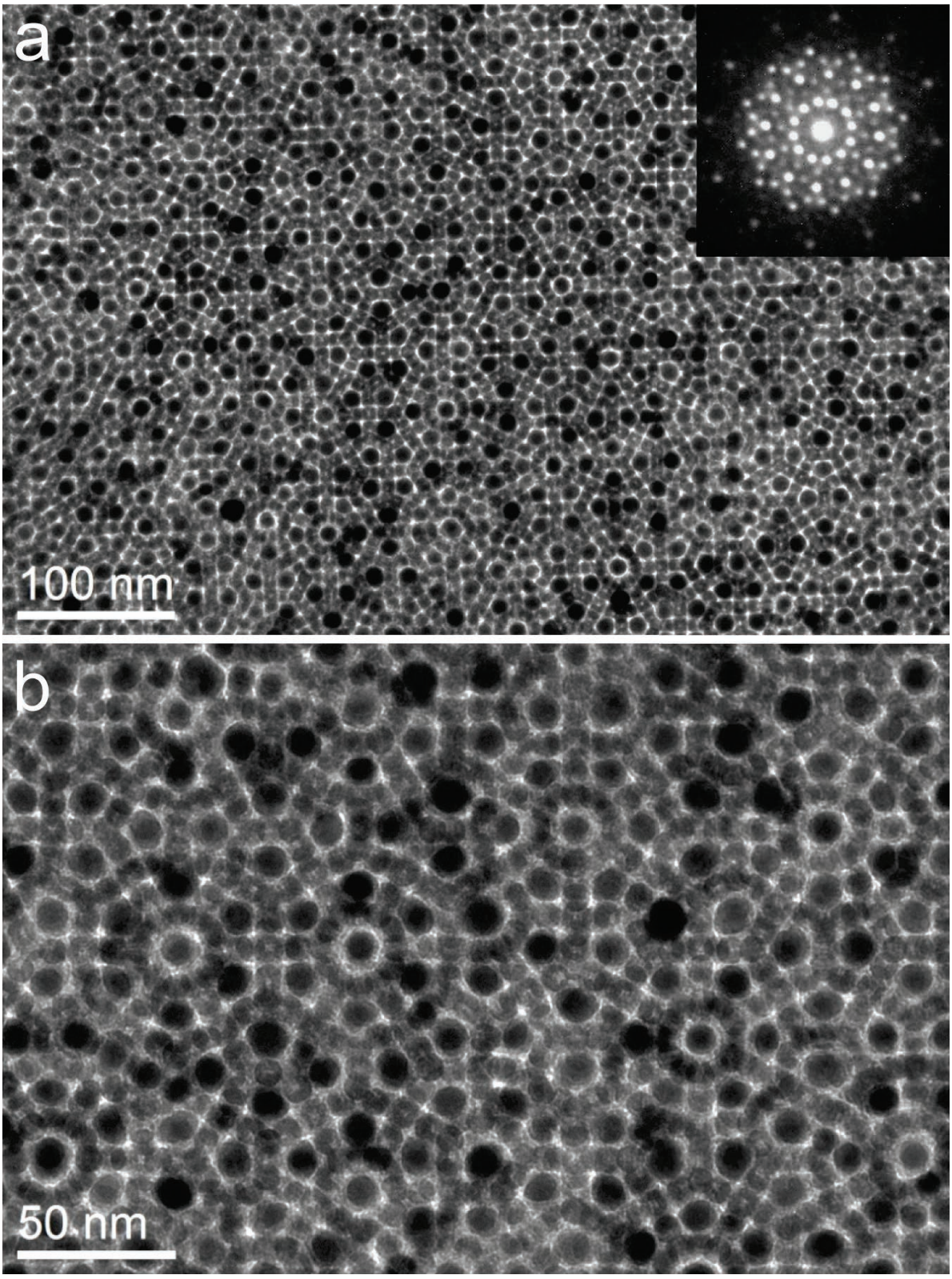

Supplementary Figure 5. (a) Low-magnification and corresponding SAED pattern (inset) and (b) high-magnification TEM images of DDQCs self-assembled from 8.8 nm Fe_3O_4 and 14.6 nm Fe_3O_4 NCs.

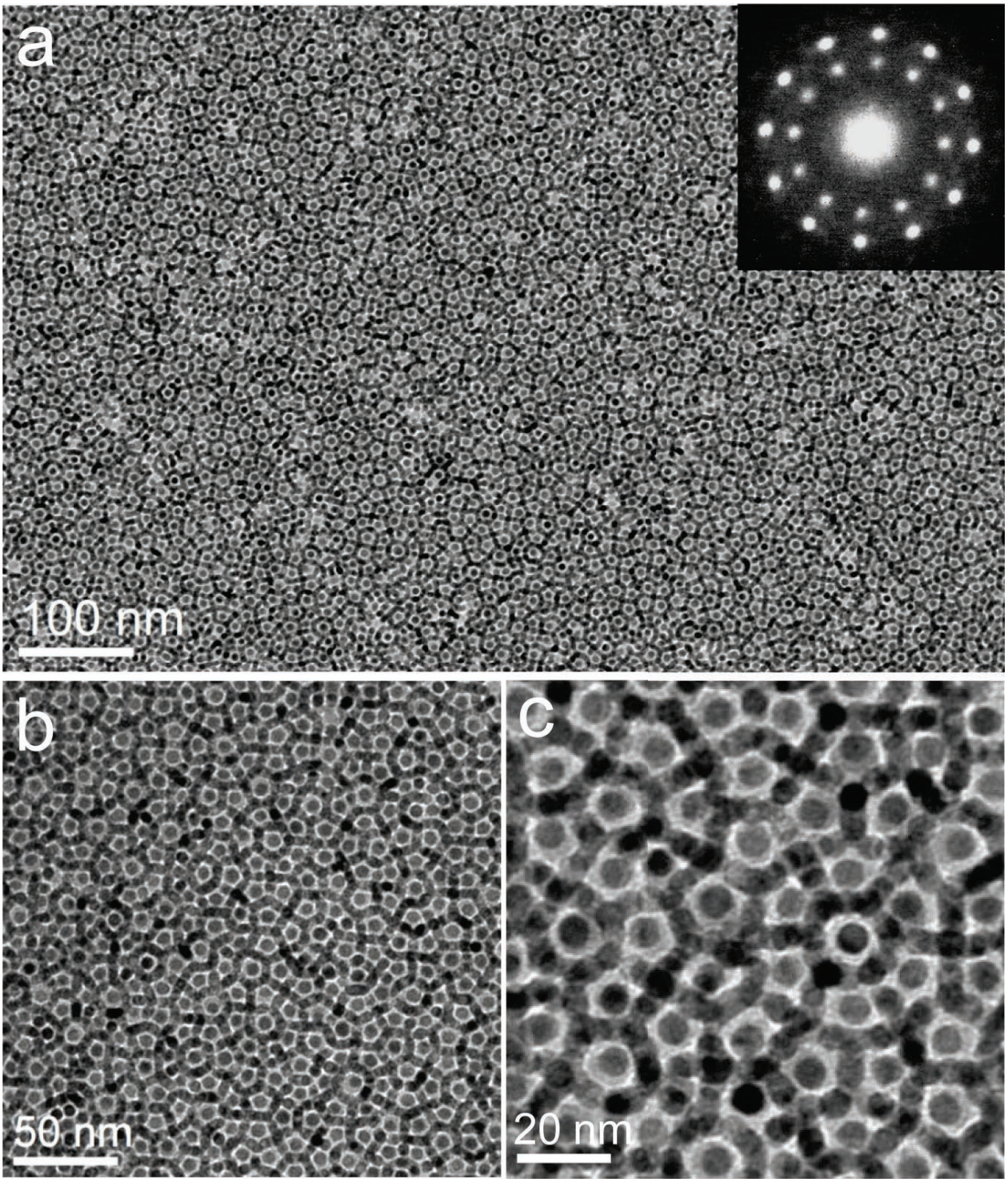

Supplementary Figure 6. (a) Low-magnification and corresponding SAED pattern (inset) and (b,c) high-magnification TEM images of DDQCs self-assembled from 5.8 nm Au and 9.7 nm Fe_3O_4 NCs.

DOI: 10.1038/NMAT4759

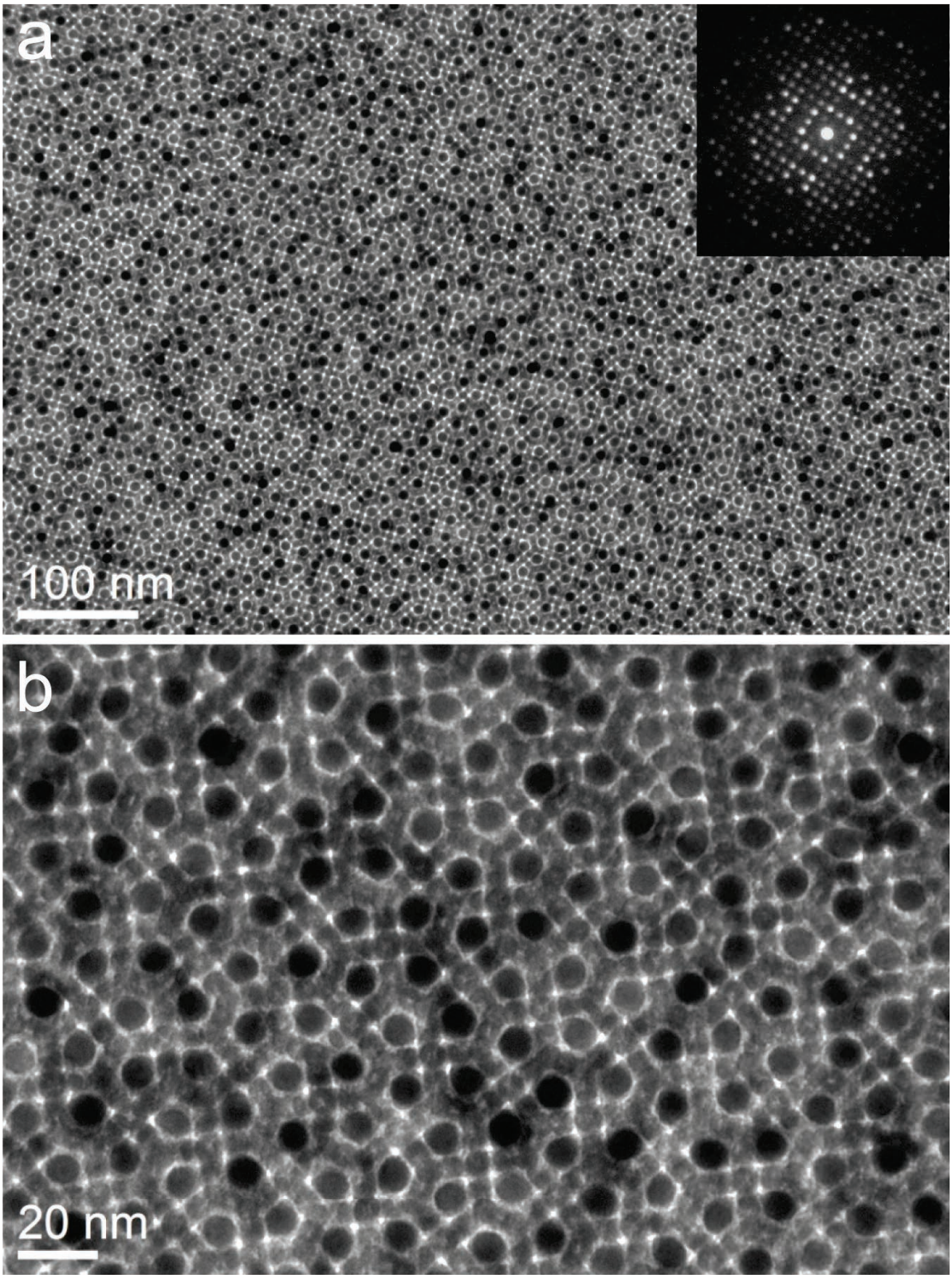

Supplementary Figure 7. (a) Low-magnification and corresponding SAED pattern (inset) and (b) high-magnification TEM images of σ-phase BNSLs self-assembled from 6.8 nm $CoFe_2O_4$ and 12.0 nm Fe_3O_4 NCs.

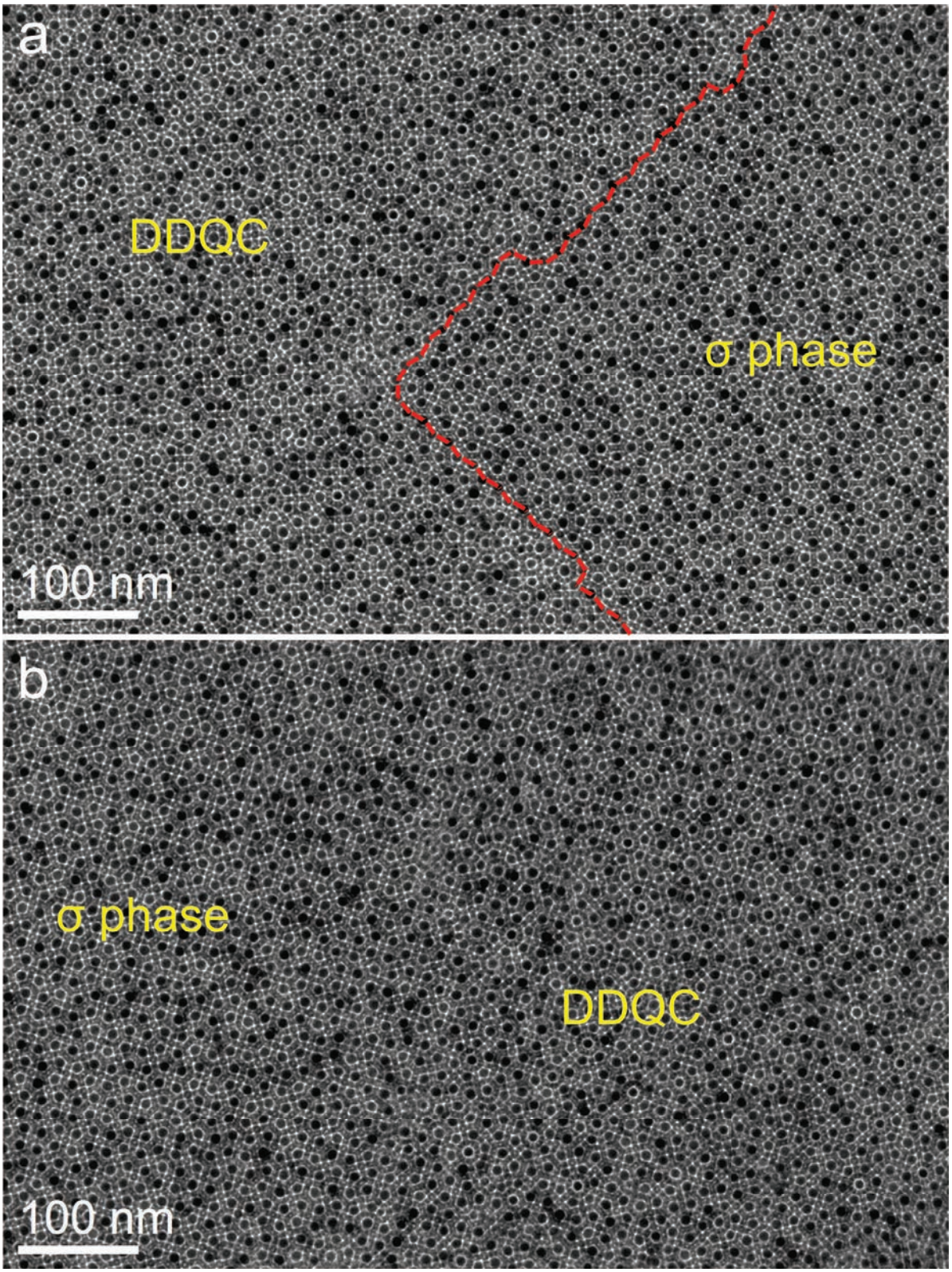

Supplementary Figure 8. (a,b) TEM images showing the coexistence of quasicrystalline and σ-phase domains in BNSLs self-assembled from 6.8 nm $CoFe_2O_4$ and 12.0 nm Fe_3O_4 NCs. The red dashed line in (a) delineates the boundary between quasicrystalline and σ-phase domains.

DOI: 10.1038/NMAT4759

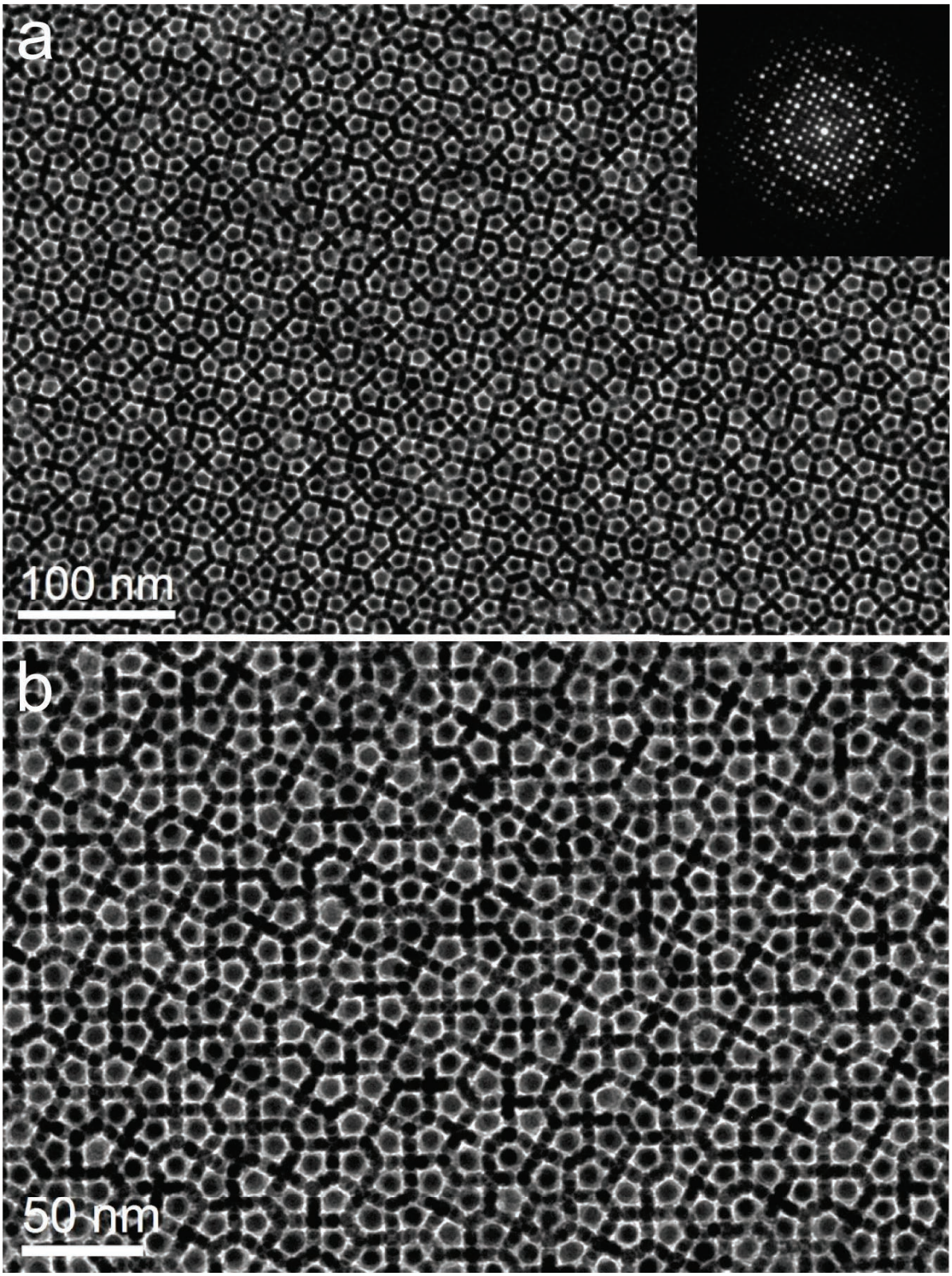

Supplementary Figure 9. (a) Low-magnification and corresponding SAED pattern (inset) and (b) high-magnification TEM images of σ-phase BNSLs self-assembled from 6.2 nm FePt and 11.5 nm Fe_3O_4 NCs.

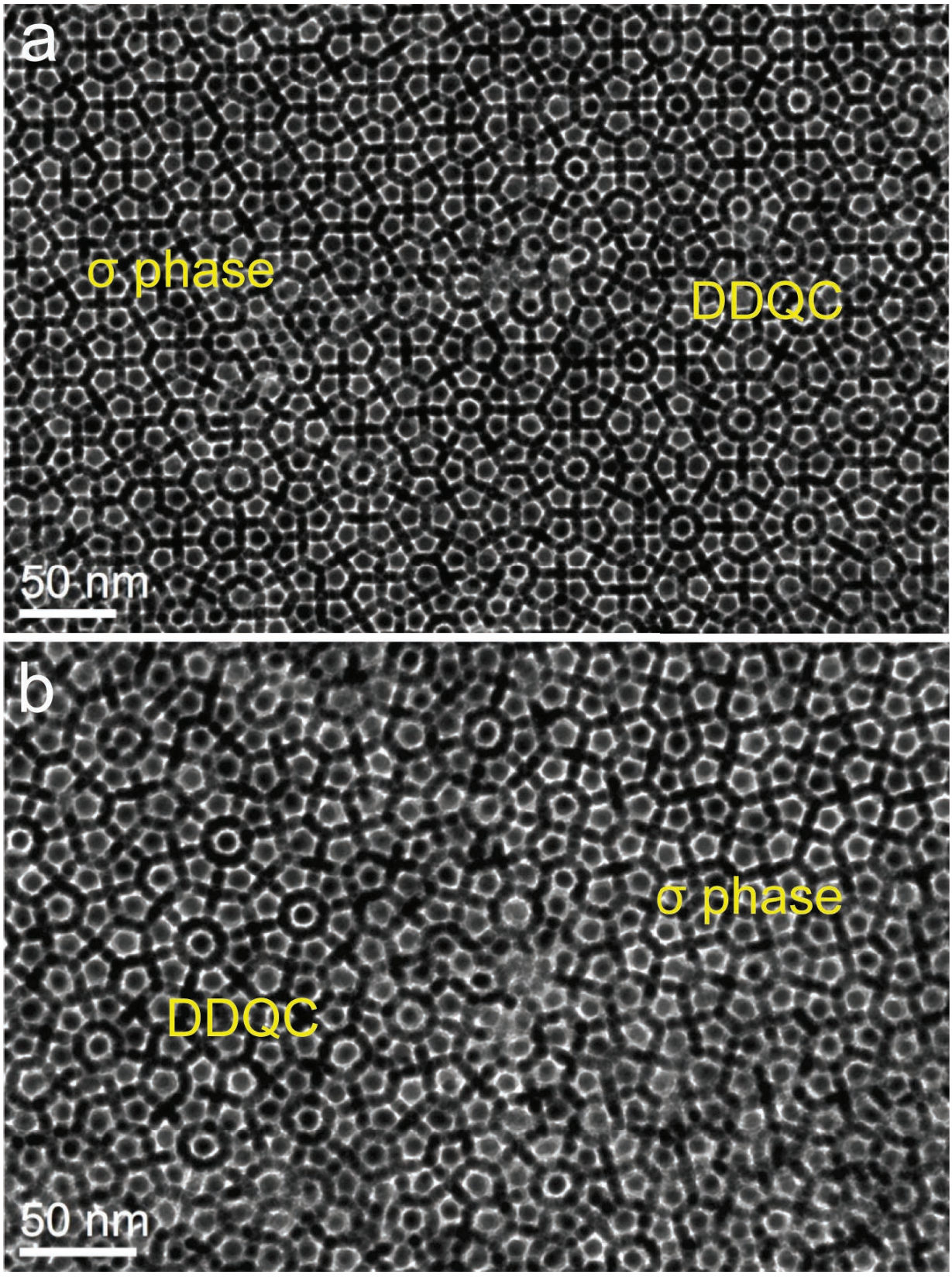

Supplementary Figure 10. (a,b) TEM images showing the coexistence of quasicrystalline and σ-phase domains in BNSLs self-assembled from 6.2 nm FePt and 11.5 nm Fe_3O_4 NCs.

DOI: 10.1038/NMAT4759

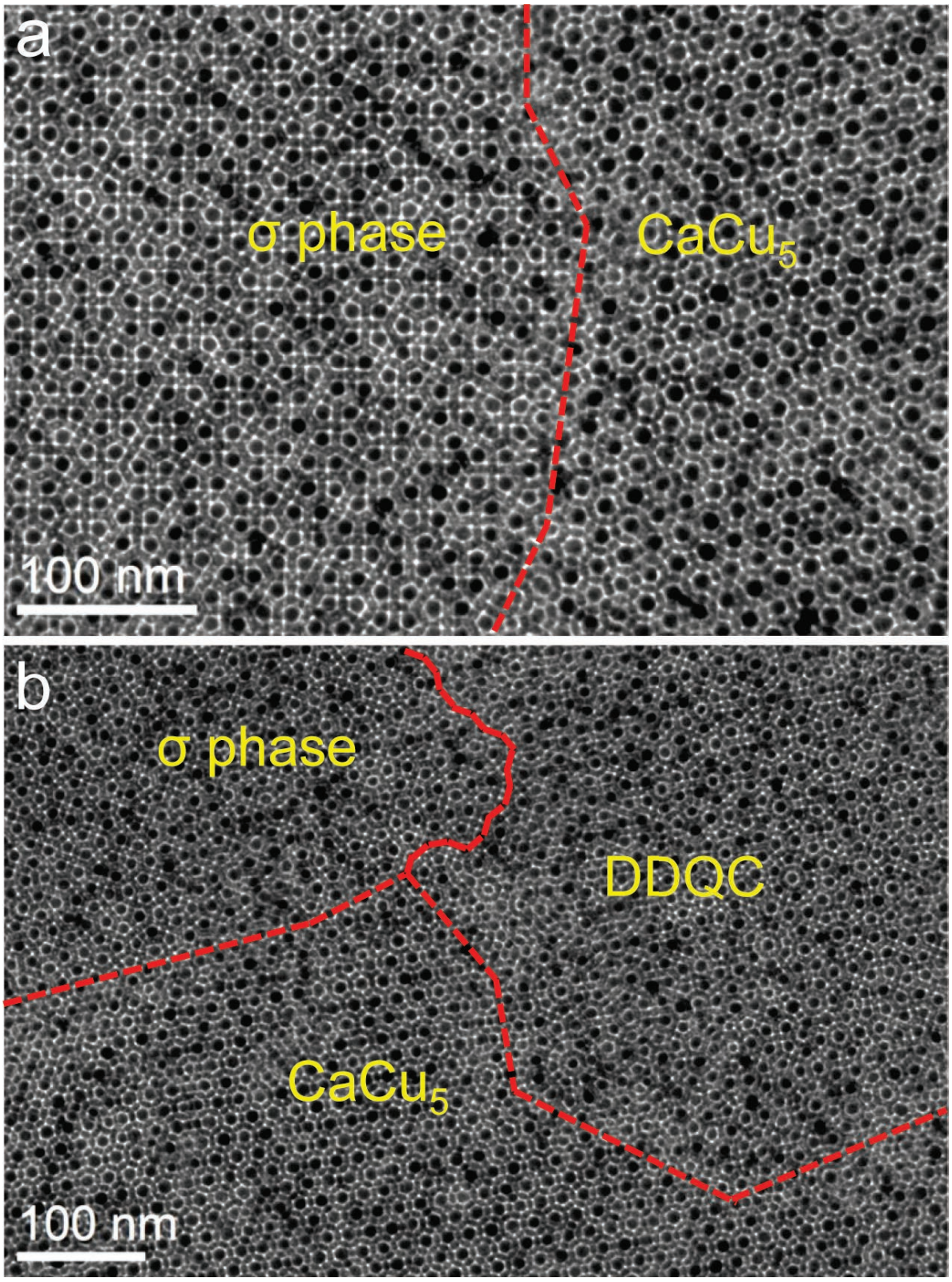

Supplementary Figure 11. (a,b) TEM images showing the coexistence of quasicrystalline, σ-phase and $CaCu_5$-type domains in BNSLs self-assembled from 6.8 nm $CoFe_2O_4$ and 12.0 nm Fe_3O_4 NCs. The red dashed lines delineate grain boundaries.

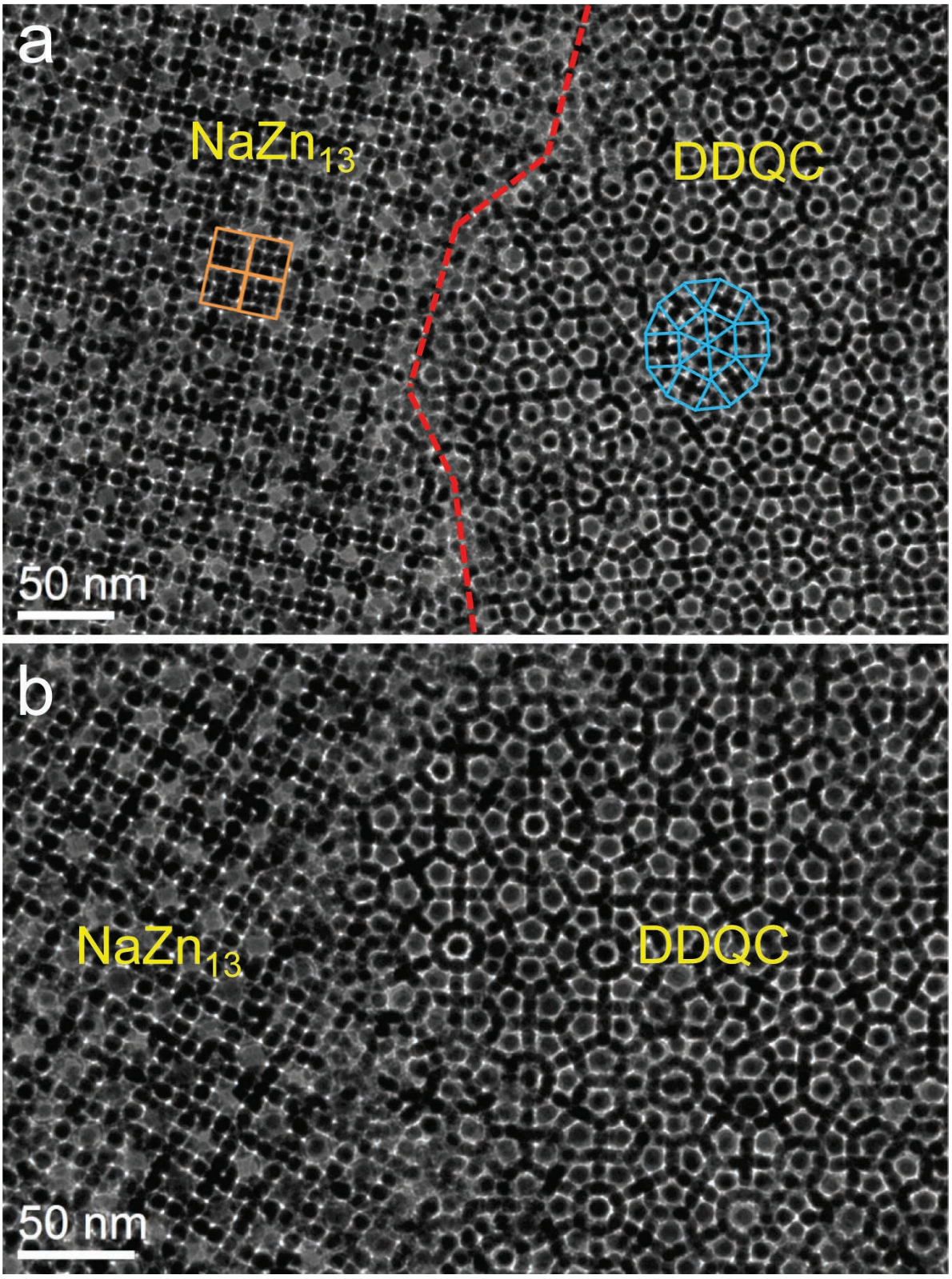

Supplementary Figure 12. (a,b) TEM images showing the coexistence of quasicrystalline and $NaZn_{13}$-type domains in BNSLs self-assembled from 6.2 nm FePt and 11.5 nm Fe_3O_4 NCs. The red dashed line in (a) delineates the grain boundary.

DOI: 10.1038/NMAT4759

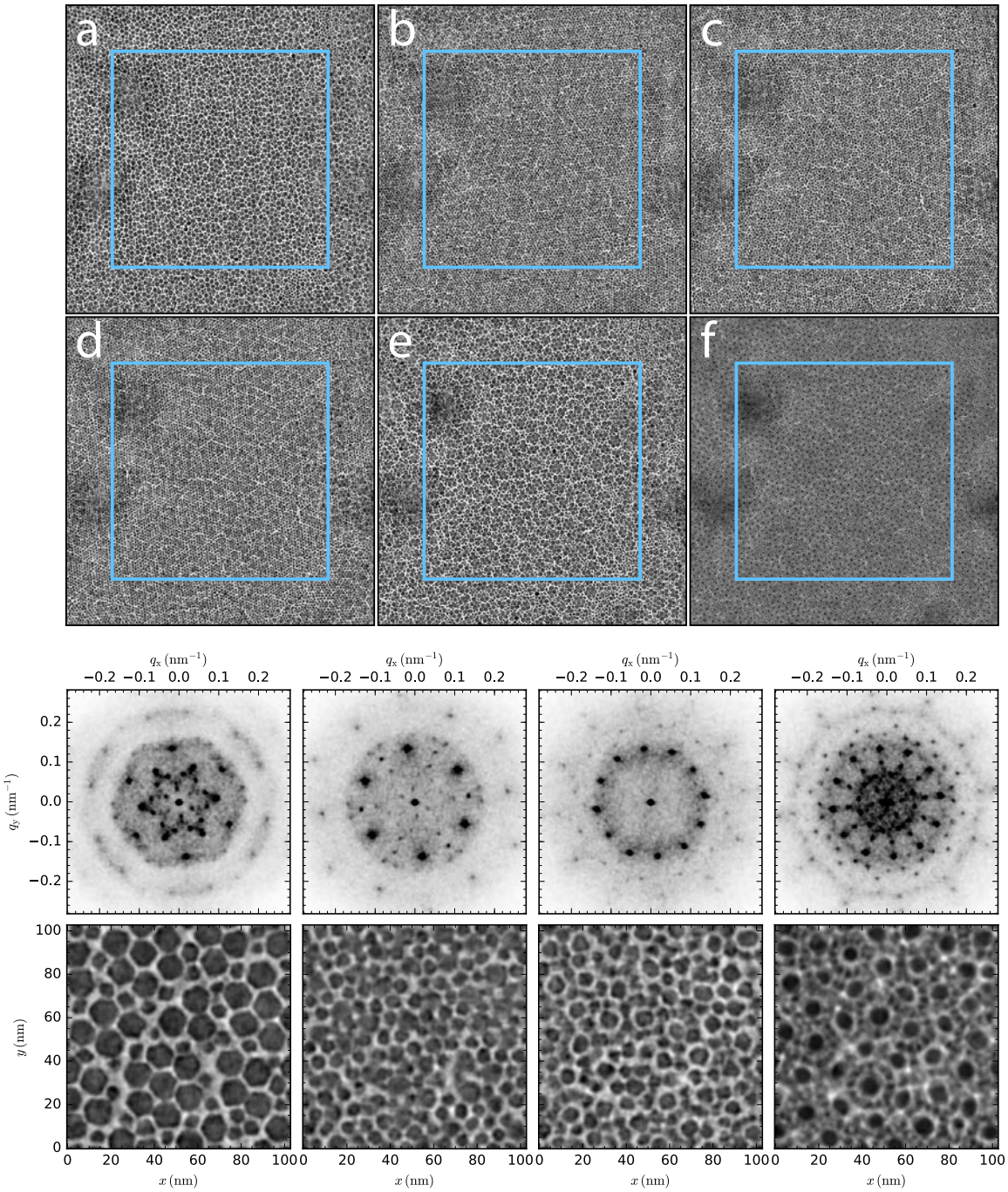

Supplementary Figure 13. Top: Full tomographic slices for the $CoFe_2O_4$-Fe_3O_4 sample shown in Fig. 2 and in Supplementary Movie 1. The figure shows the tomography slices numbering (from the bottom of the sample) (a) 50, (b) 59, (c) 64, (d) 68, and (e) 77 corresponding to a M, P, T, P′, M′ layer, respectively. Layers 50 to 103 are projected together in (f). The inset squares show the region Fourier transformed for figure 2 in the main text. Bottom: Fourier transforms of the images in (a), (b), (c), (f), and corresponding cross-sectional images (for a-c) or projection image (for f) with increased magnifications. The full tomographic resolution is 0.64 nm per pixel. Dominant peaks seen in the Fourier transforms of the P and T layers are due to nearest neighbor interparticle correlations.

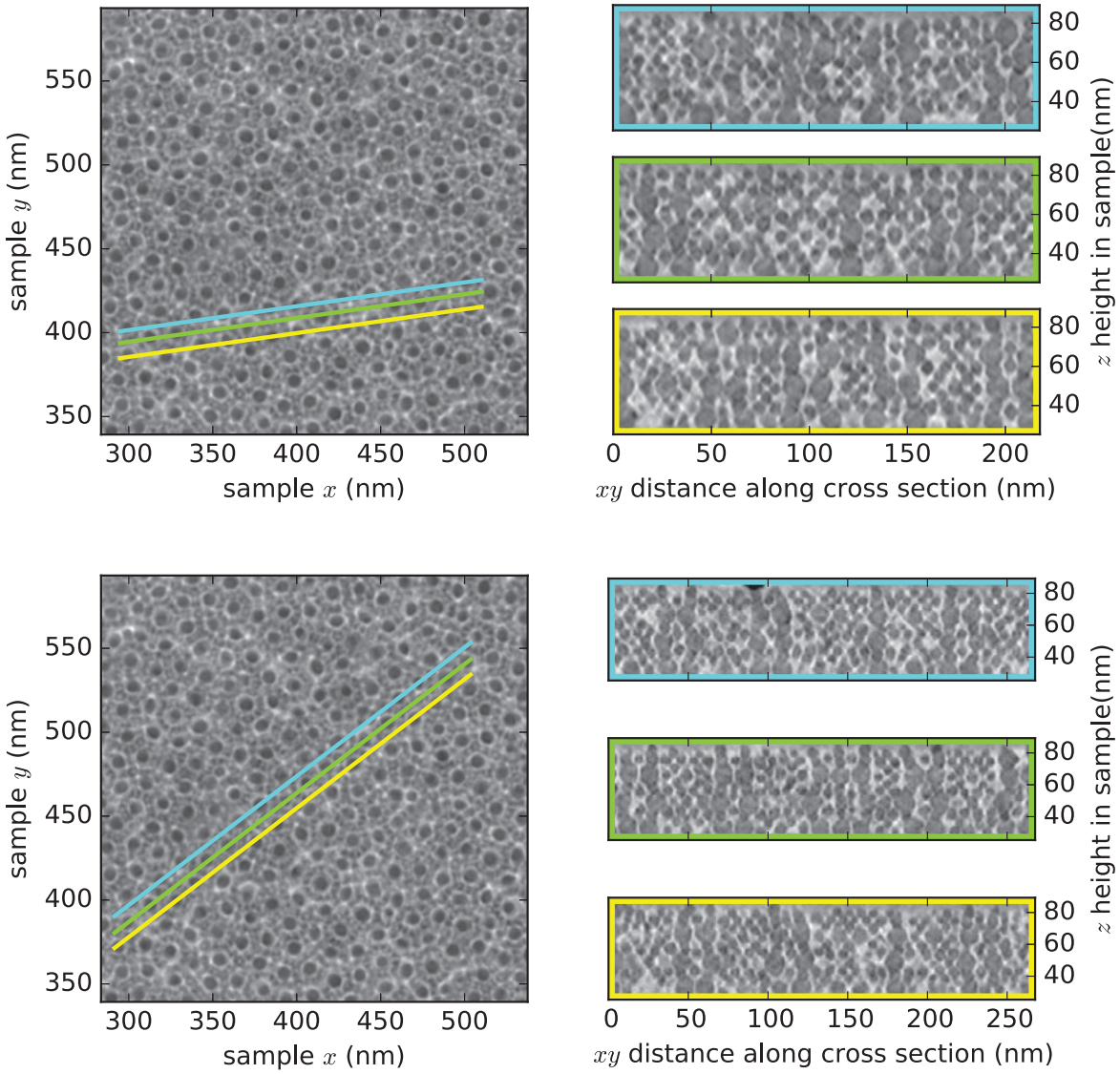

Supplementary Figure 14. Projection images along the dodecagonal axis (left) and cross-sectional slices (right) of a subset of the tomographic reconstruction data of Supplementary Figure 13. The slice paths are indicated as lines on the projection image, color coded to the borders of the cross-sectional slices shown on the right. Staggered columns of large nanocrystals as well as distortions in the structure necessitated by certain tile configurations are visible. The projection images on the left correspond to one unit cell thickness from M to the next M layer, which is about 53 slices or 34 nm. The cross-sectional images on the right show the full thickness of the sample, which is slightly less than twice of the periodicity along the dodecagonal direction (*z*-axis).

DOI: 10.1038/NMAT4759

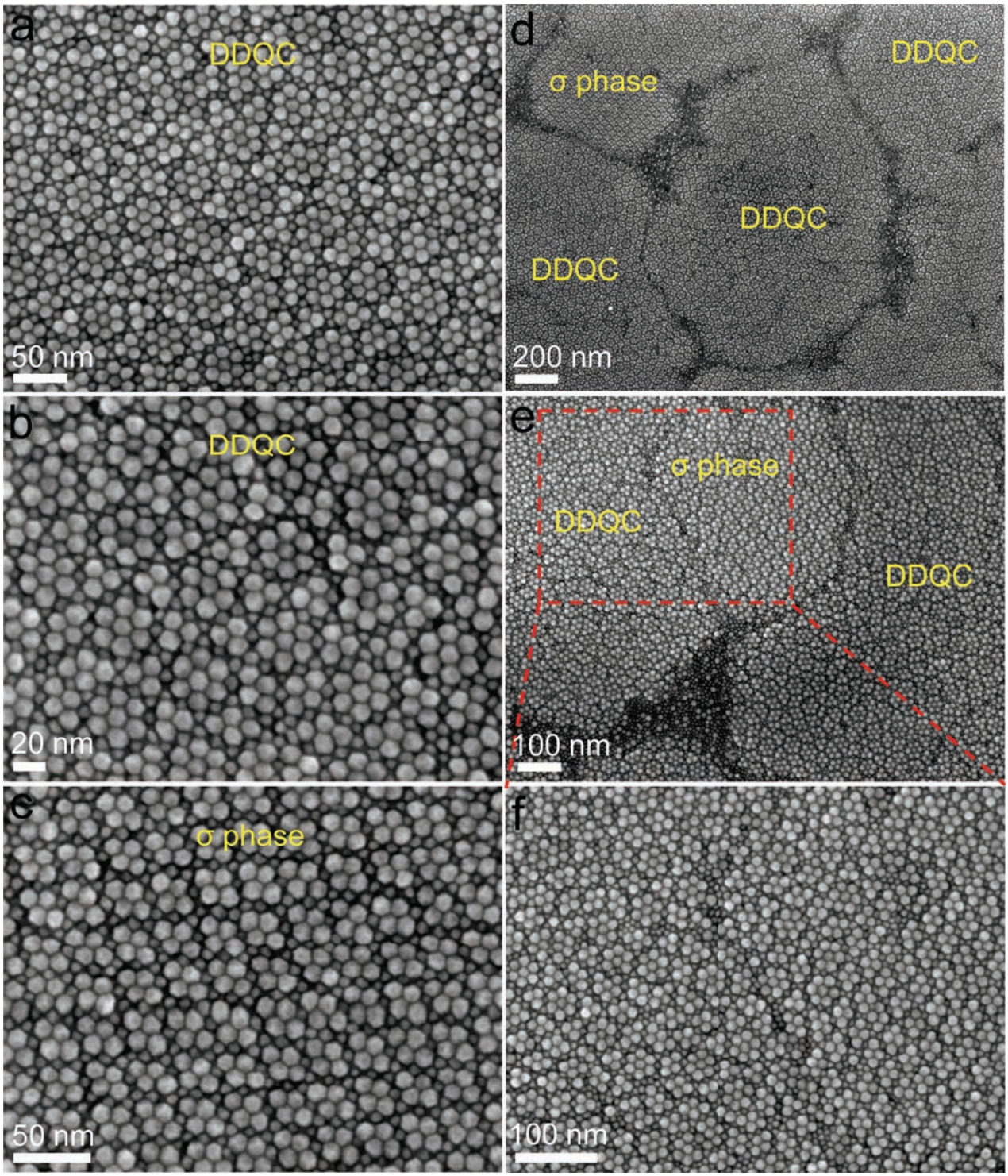

Supplementary Figure 15. SEM images showing the surface topography of (a,b) quasicrystalline and (c) σ-phase BNSL domains self-assembled from 6.8 nm $CoFe_2O_4$ and 12.0 nm Fe_3O_4 NCs. (d,e) Low-magnification and (f) high-magnification SEM images showing the coexistence of quasicrystalline and σ-phase BNSLs.

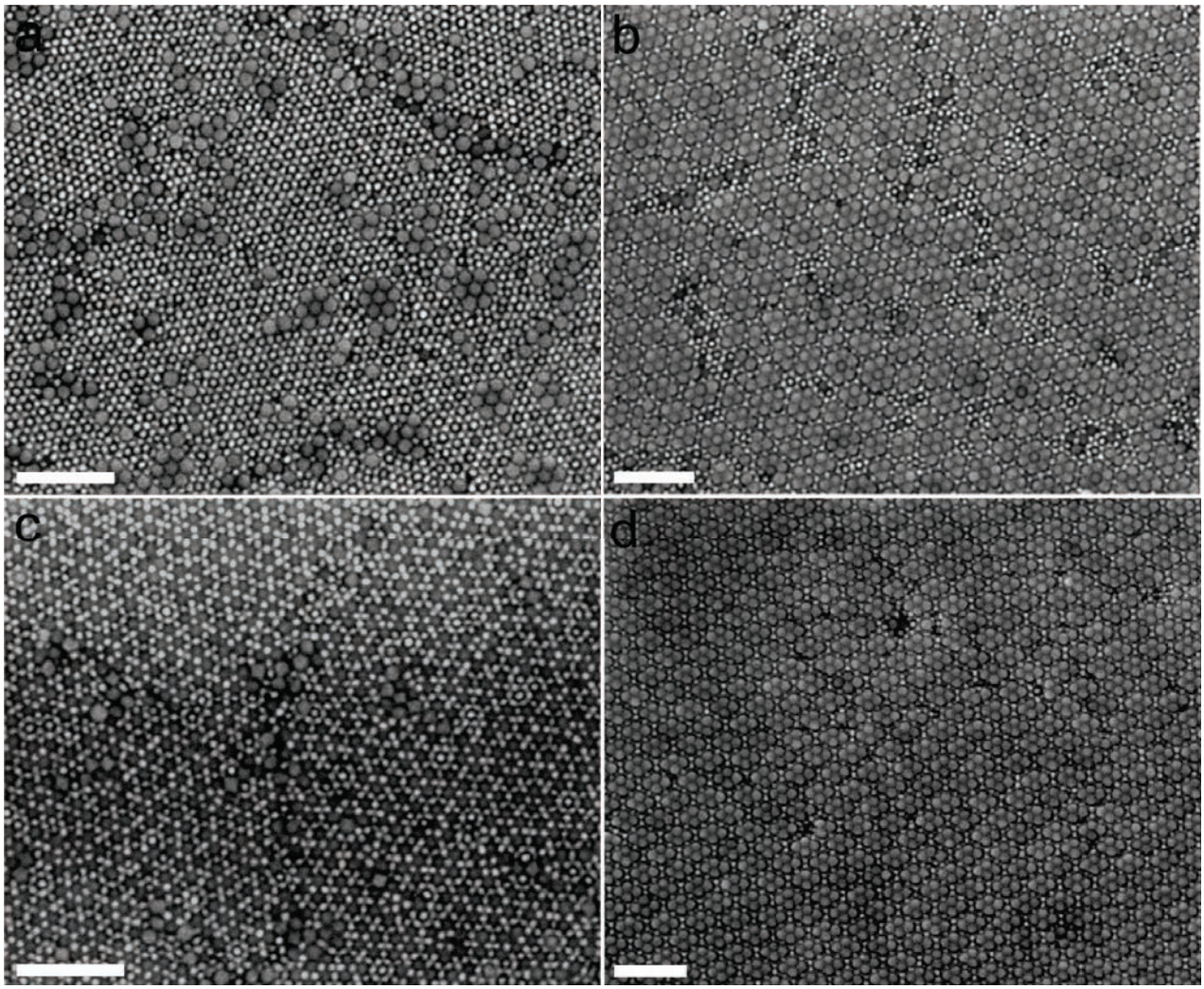

Supplementary Figure 16. (a-c) Low-magnification SEM images showing the surface topography of quasicrystalline domains with different surface terminations and (d) low-magnification SEM image of σ-phase BNSL domains self-assembled from 6.2 nm FePt and 11.5 nm Fe_3O_4 NCs. All scale bars represent 100 nm.

DOI: 10.1038/NMAT4759

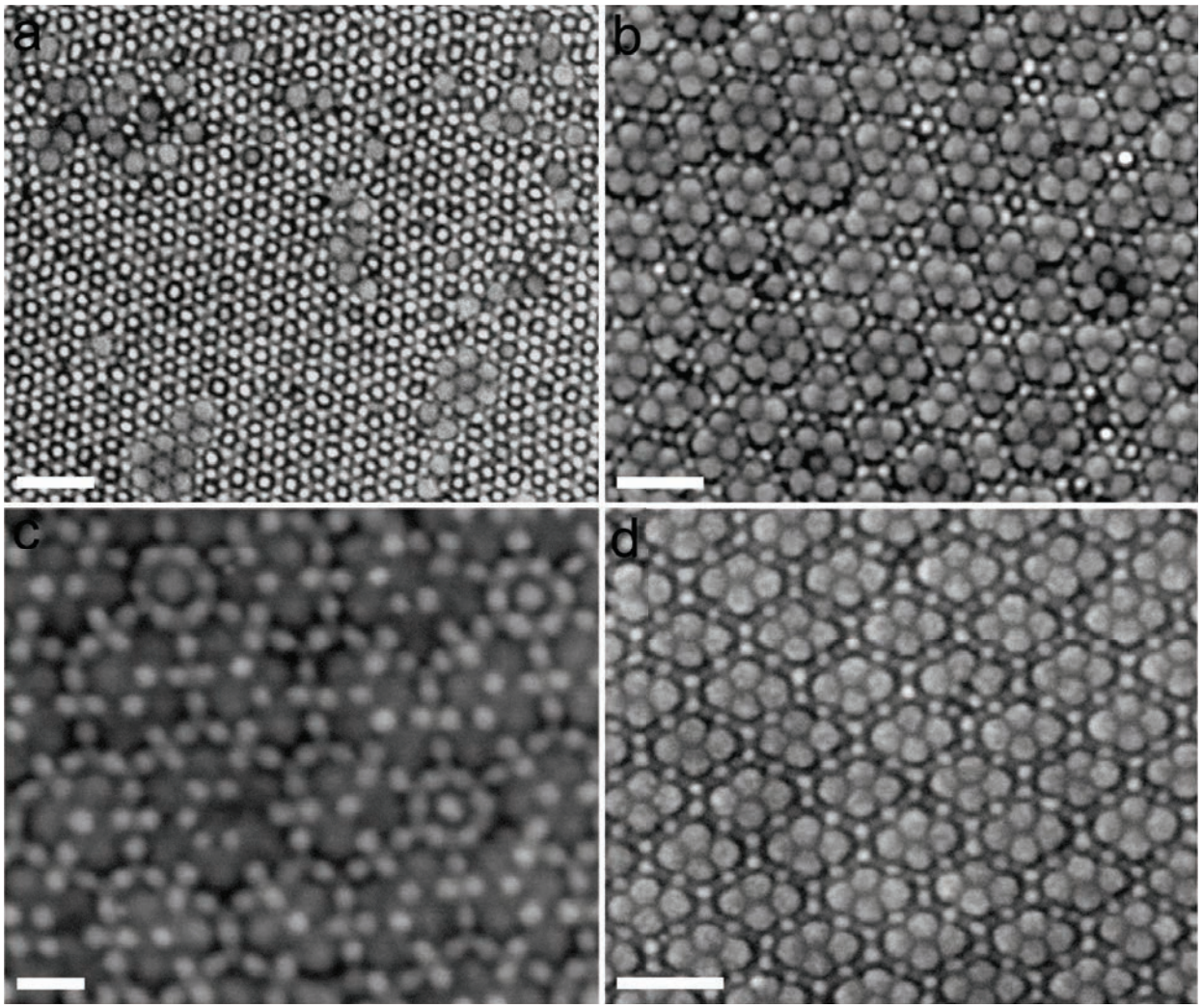

Supplementary Figure 17. (a-c) High-magnification SEM images showing the surface topography of quasicrystalline domains with different surface terminations and (d) high-magnification SEM image of σ-phase BNSL domains self-assembled from 6.2 nm FePt and 11.5 nm Fe_3O_4 NCs. Scale bars: (a, b, d) 50 nm, (c) 20 nm.

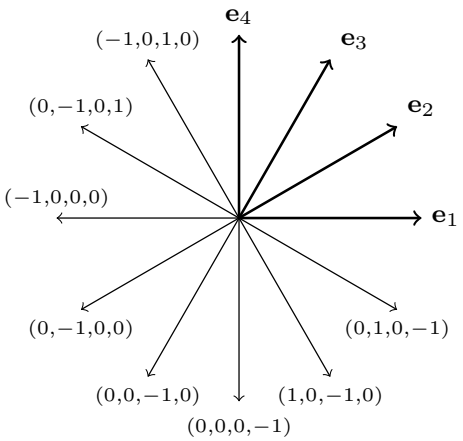

Supplementary Figure 18. The twelve possible tiling edge vectors are integer linear combinations of the four quasi-lattice basis vectors $\mathbf{e}_1$, $\mathbf{e}_2$, $\mathbf{e}_3$, $\mathbf{e}_4$.

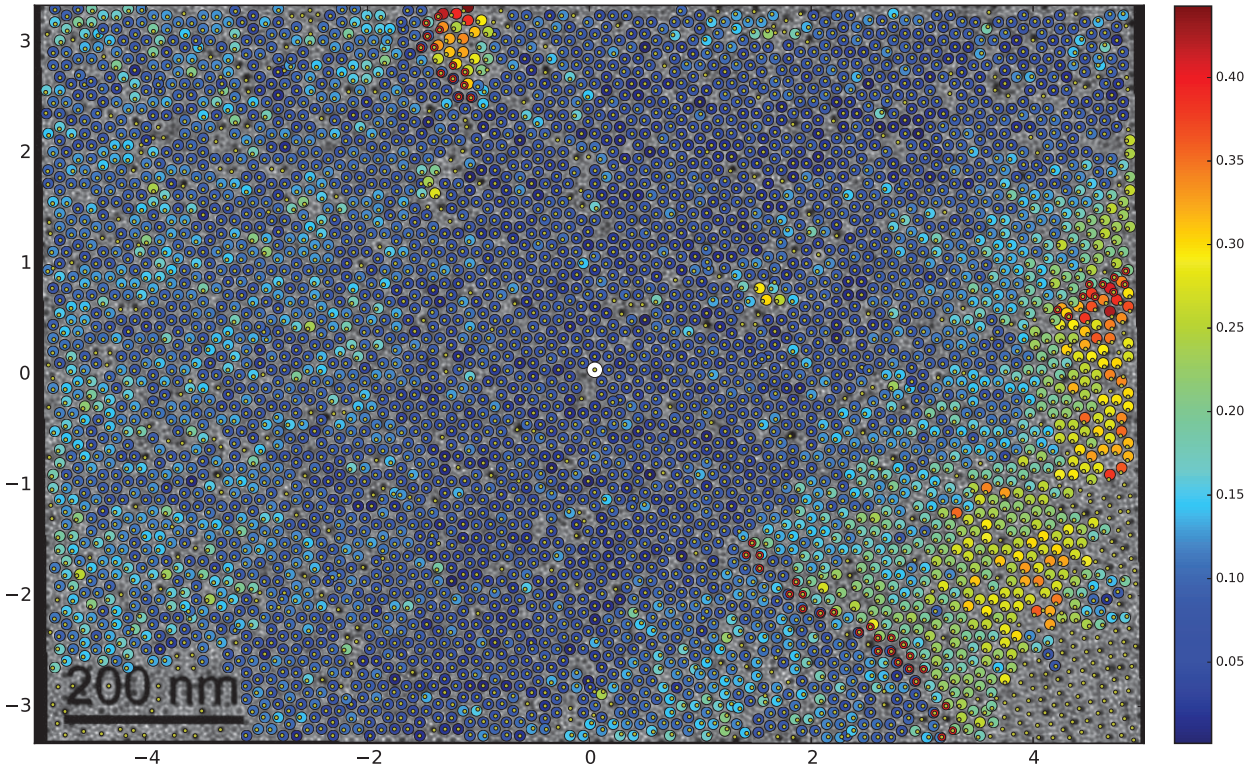

Supplementary Figure 19. Illustration of the tiling vertex detection workflow. The network exploration began at the coordinate marked by the large white dot. The image shows the detected vertices overlaid on the TEM image. The color of a vertex corresponds to the distance between the detected position $\mathbf{t}_i$ and the position reconstructed using its four-dimensional coordinates $\mathbf{P}^{\parallel}\mathbf{t}_i{}^{(4)}$.

DOI: 10.1038/NMAT4759

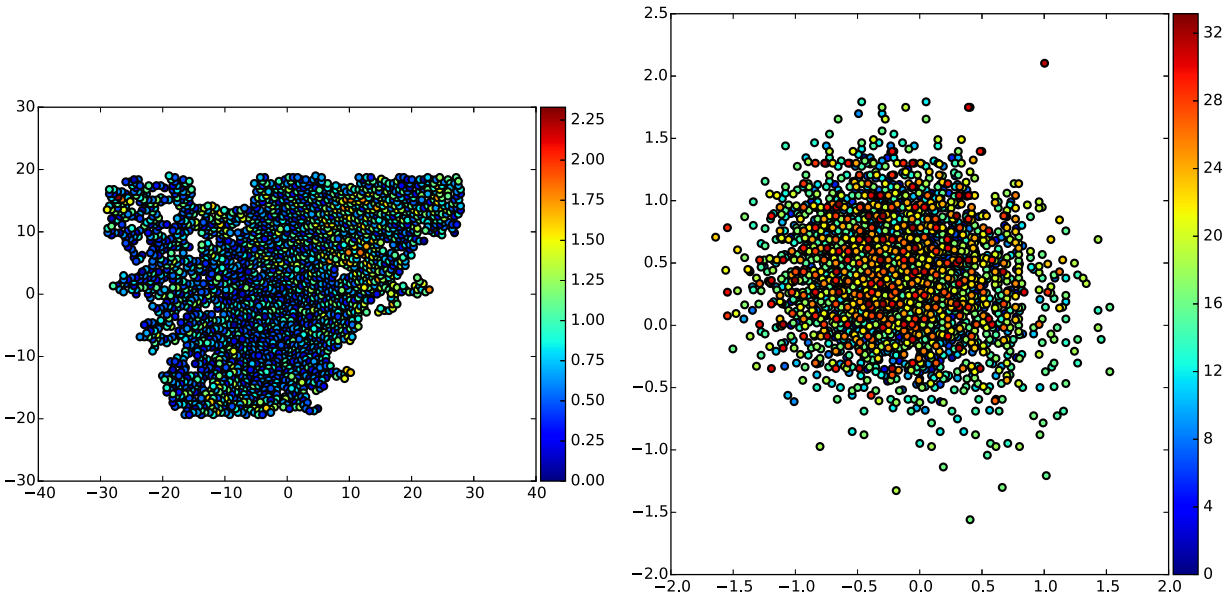

Supplementary Figure 20. Tile vertices of the experimental tiling in parallel space (left) and projected on perpendicular space (right). The vertices are colored by distance to a reference point in the other space. The occupation domain formed by the tile vertices in perpendicular space is roughly circular and thermally broadened.

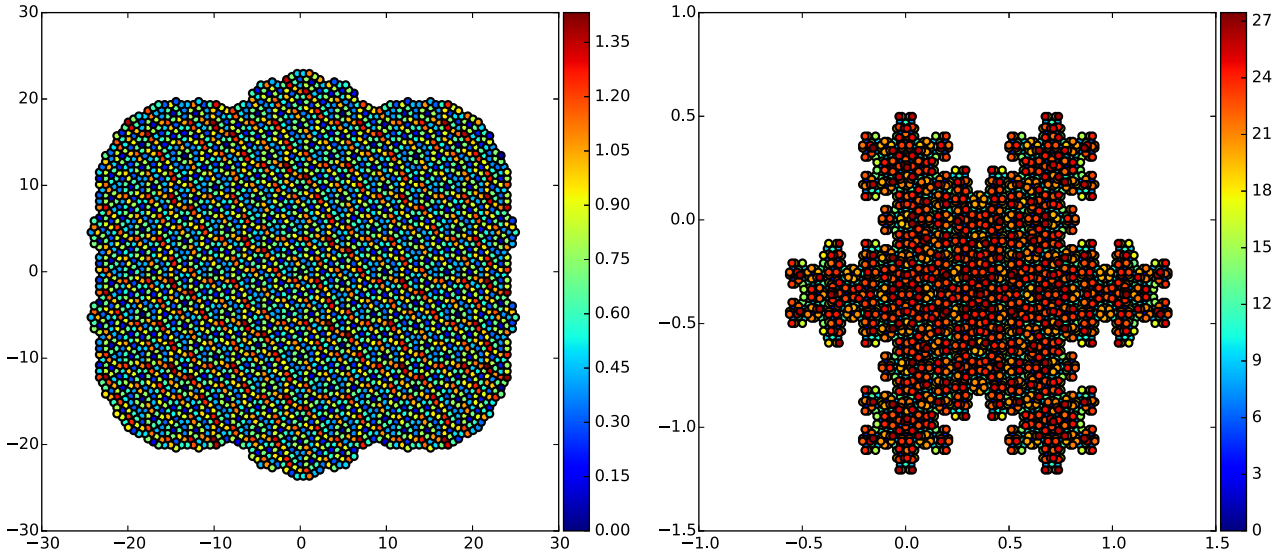

Supplementary Figure 21. Tile vertices of an ideal, generated square-triangle tiling projected in parallel (left) and perpendicular (right) space. The vertices are colored by distance to a reference point in the other two dimensions. The set of points form a fractal occupation domain with 6-fold symmetry in perpendicular space.

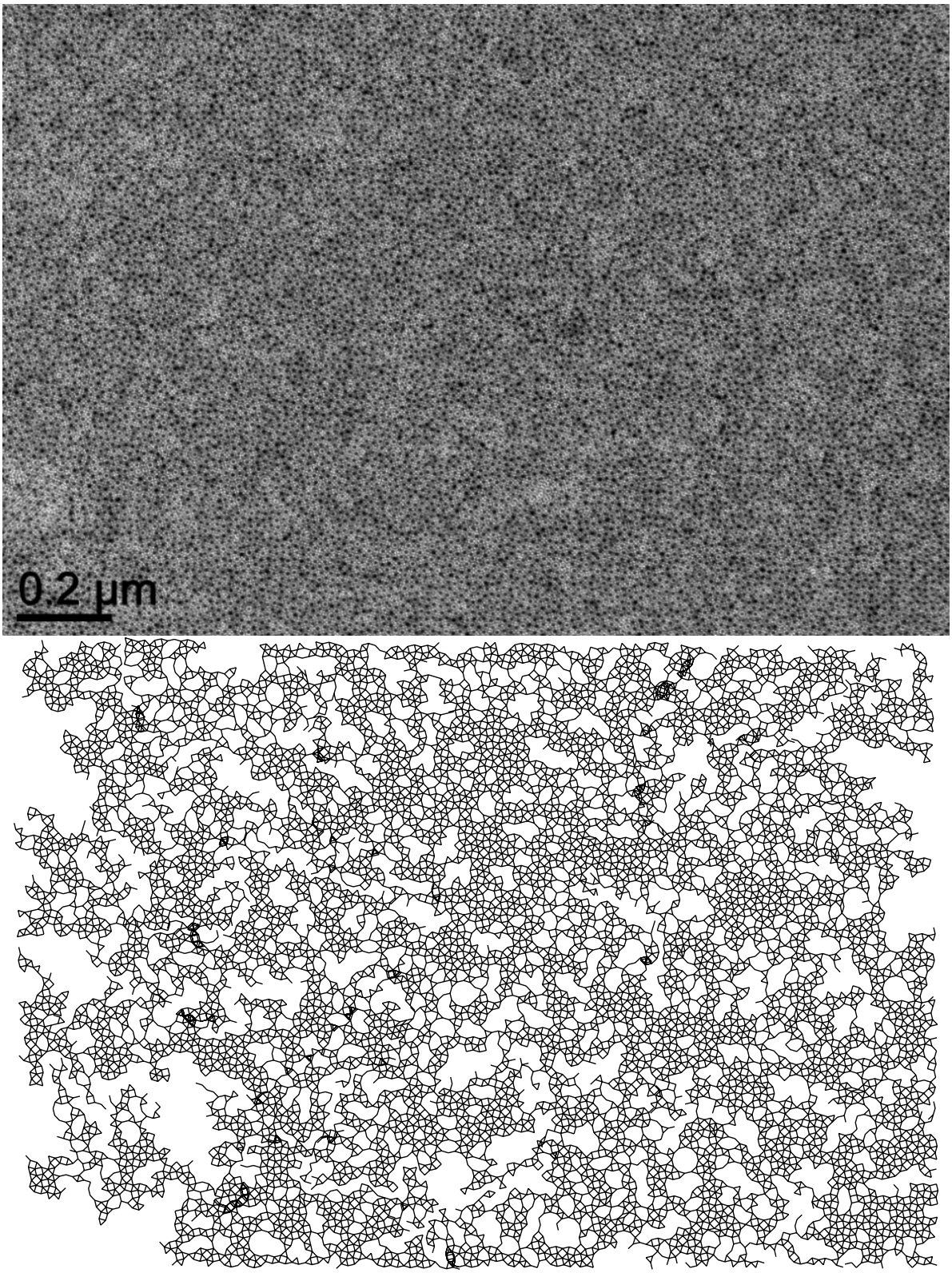

Supplementary Figure 22. Sample C (see Fig. 3f) contains several regions with insufficient contrast for the automatic tiling analysis. Still, our algorithm is able to obtain self-consistent tile coordinates. Note also the occurrences of small σ-phase regions, e.g., in the bottom right.

DOI: 10.1038/NMAT4759

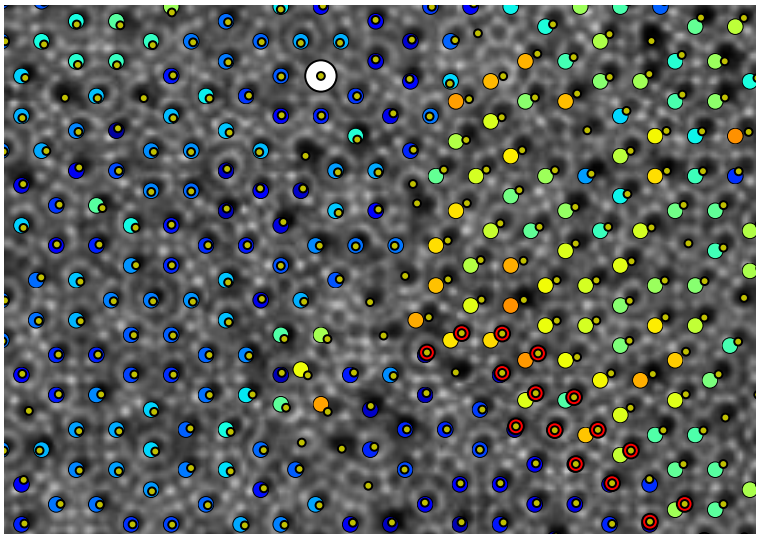

Supplementary Figure 23. The starting point of the breadth first search (large white dot) determines how coordinates around defects are explored. The detected tile vertices $\mathbf{t}_i$ are shown with small olive disks, while projected four-dimensional coordinates $\mathbf{P}^{\parallel}\mathbf{t}_i{}^{(4)}$ are shown with larger disks, colored by the distance to the detected position (see also Fig. S18). Tile vertices, which cannot be assigned unique four-dimensional coordinates because they differ depending on the search direction (lifting continuity violations), are highlighted with additional red circles. These vertices form a string ending at a dislocation.

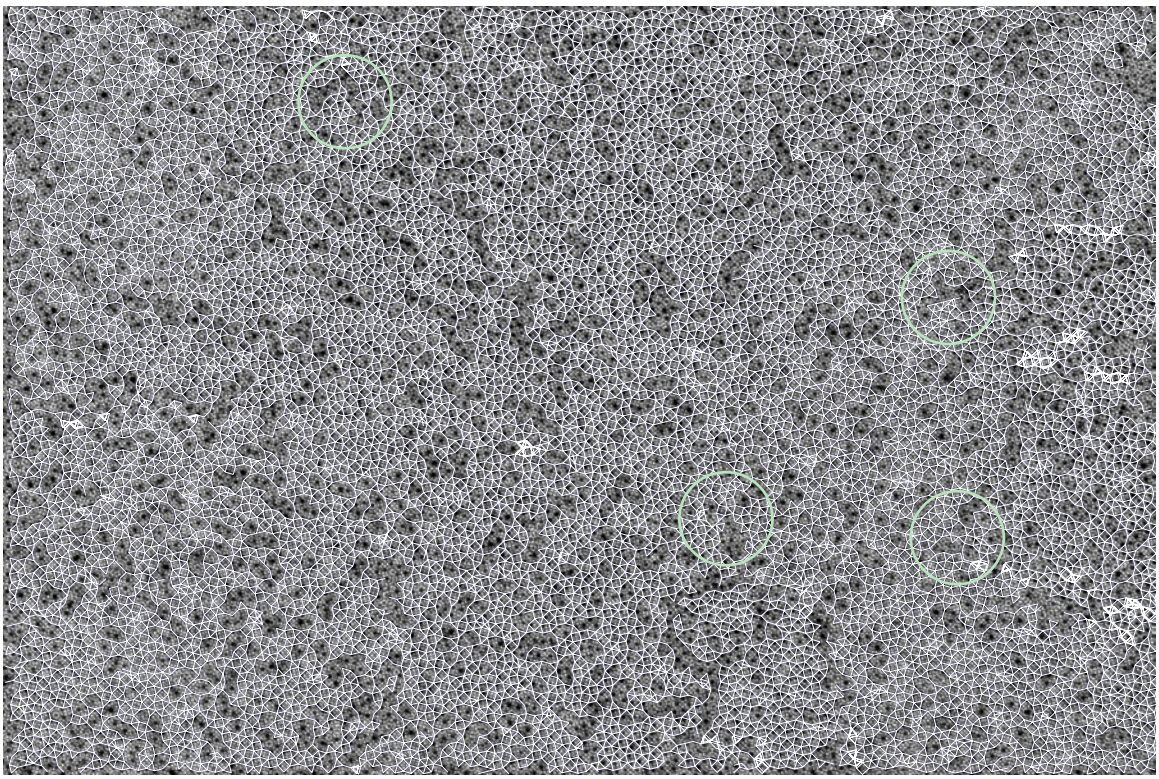

Supplementary Figure 24. Four dislocations in sample B (see Fig. 3f) are highlighted on the overlaid net.

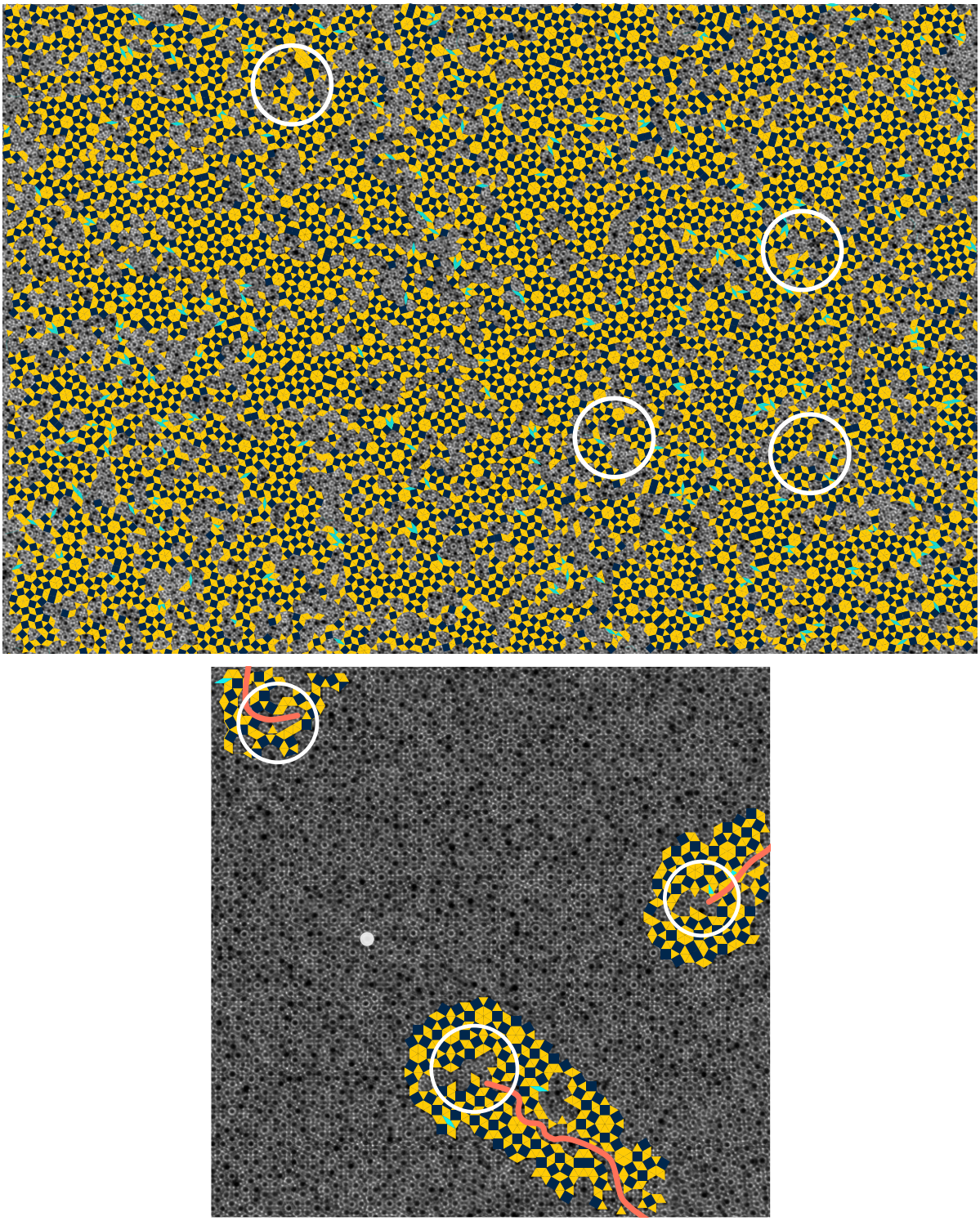

Supplementary Figure 25. Sample B (see Fig. 3f) with square, triangle, and rhomb tiles overlaid. The full field-of-view (top) and a section highlighting three dislocation cores (bottom) are shown. In the bottom figure, the white dot denotes the tile vertex where the automated network exploration was initiated. As the exploration proceeded around the noted dislocations, the topology of the dislocations produced disagreeing tile coordinates. We highlight the strings of lifting continuity violations with thick light red lines.

DOI: 10.1038/NMAT4759

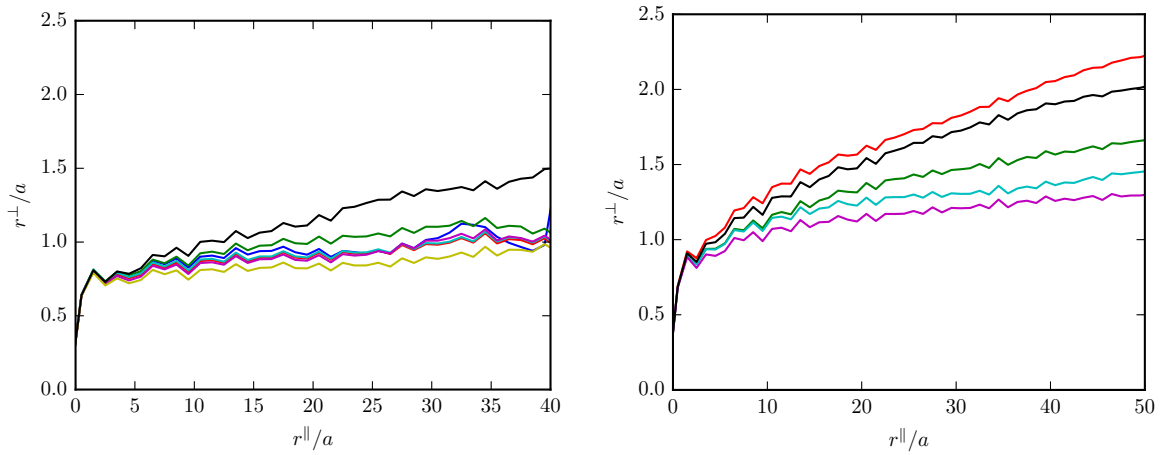

Supplementary Figure 26. Phason displacement analysis of the (smaller) sample A (see Fig. 3f) shown on the left and the (larger) sample B shown on the right. To analyze the robustness of the analysis we show curves starting from different tile vertices. A slight variation is observed but the general shape of the curve remains unchanged.

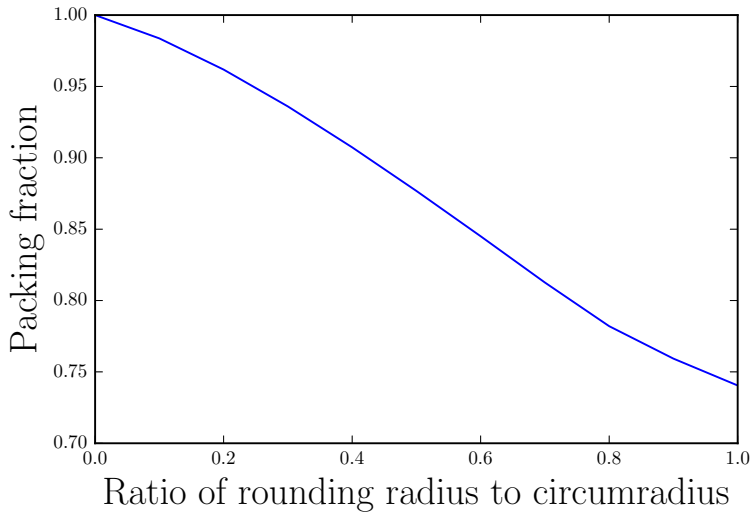

Supplementary Figure 27. Maximum packing fraction for sphero-truncated octahedra interpolating between the truncated octahedron (Archimedean solid, rounding radius 0.0) and the sphere (rounding radius 1.0). Agreement was found with boxes of 1, 2, 3, and 4 particles, implying that the densest packing contains only a single particle. The primitive unit cell transforms continuously from the BCC lattice, preferred by truncated octahedra, to the FCC lattice, preferred by spheres.

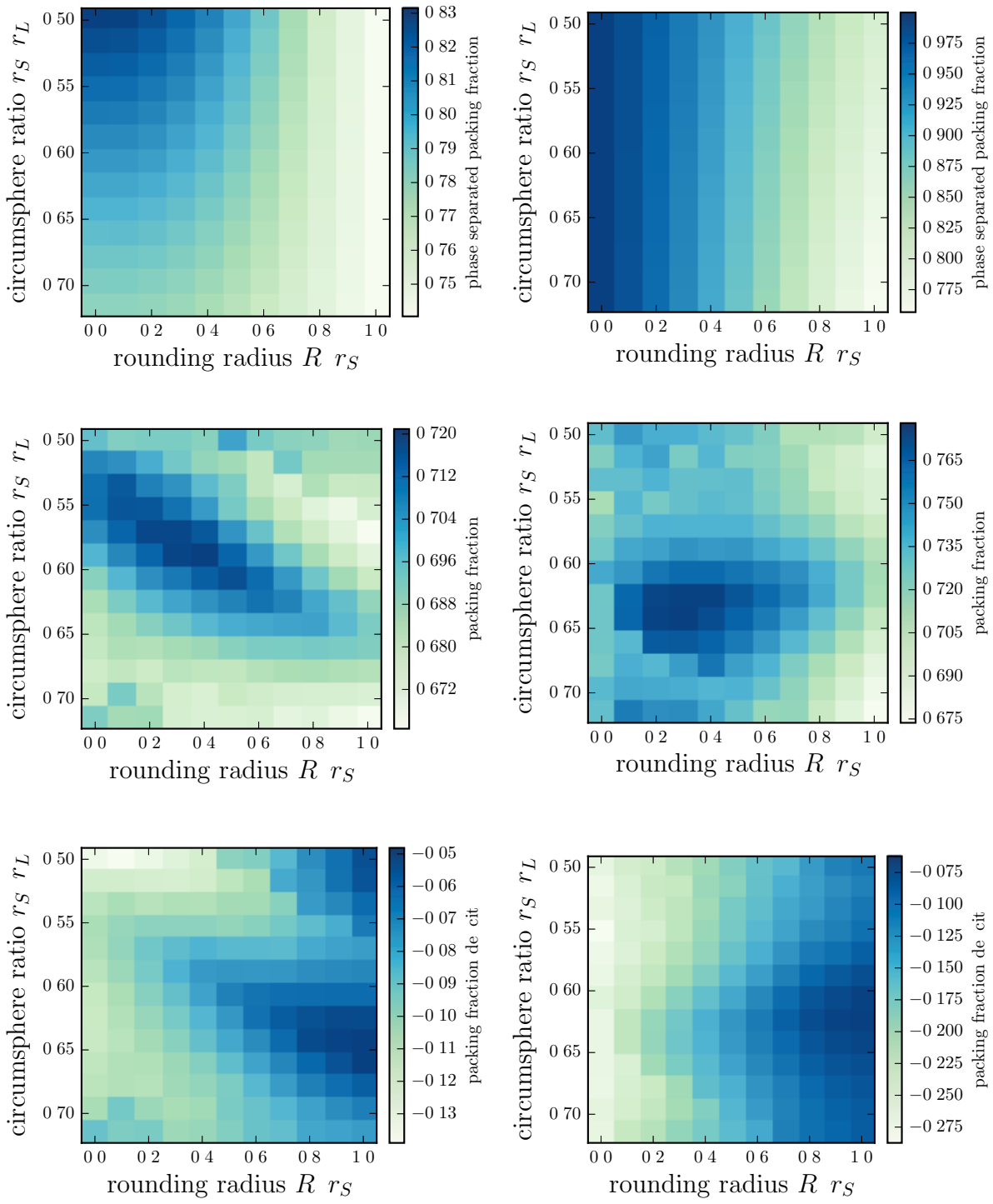

Supplementary Figure 28. Calculated maximum packing fractions. We compare mixtures of sphero-truncated octahedra and smaller spherical particles (left), and mixtures of sphero-truncated octahedra of different sizes (right), in the phase separated state (top row), in the σ-phase (middle row), as well as the difference between the two (bottom row). In all cases, the 15:2 particle number ratio of the σ-phase (i.e. $AB_{7.5}$) was used. The densest packings of 0.721 (0.780) occurred at the circumsphere ratio of about 0.571 (0.625) and the rounding ratio of 0.4 (0.3) in the middle left (middle right).

DOI: 10.1038/NMAT4759

Movie Legends

Supplementary Movie 1. Electron tomographic reconstruction of a DDQC self-assembled from 6.8 nm $CoFe_2O_4$ and 12.0 nm Fe_3O_4 NCs. The movie scans from sample top to bottom. Citrate-stabilized Au NCs that were used as fiducial markers are visible at the beginning of this movie. The scale bar represents 20 nm.

Supplementary Movie 2. Additional electron tomographic reconstruction of a DDQC self-assembled from 6.8 nm $CoFe_2O_4$ and 12.0 nm Fe_3O_4 NCs. The movie scans from sample top to bottom. Citrate-stabilized Au NCs that were used as fiducial markers are visible at the beginning of this movie. The scale bar represents 20 nm.

Supplementary Movie 3. Electron tomographic reconstruction of a DDQC self-assembled from 6.2 nm FePt and 11.5 nm Fe_3O_4 NCs. The movie scans from sample top to bottom. The scale bar represents 20 nm.

Supplementary Movie 4. Additional electron tomographic reconstruction of a DDQC self-assembled from 6.2 nm FePt and 11.5 nm Fe_3O_4 NCs. The movie scans from sample top to bottom. The scale bar represents 20 nm.

Supplementary Movie 5. A third electron tomographic reconstruction of a DDQC self-assembled from 6.2 nm FePt and 11.5 nm Fe_3O_4 NCs. The movie scans from sample top to bottom. The scale bar represents 20 nm.

Supplementary Movie 6. Electron tomographic reconstruction of a σ-phase self-assembled from 6.2 nm FePt and 11.5 nm Fe_3O_4 NCs. The movie scans from sample top to bottom. The scale bar represents 20 nm.

Supplementary Movie 7. A series of cross-sectional vertical (*x*-*z*) slices from the three-dimensional tomographic reconstruction of a DDQC self-assembled from 6.8 nm $CoFe_2O_4$ and 12.0 nm Fe_3O_4 NCs. The movie shows scans along the horizontal *y*-axis that is perpendicular to the twelve-fold axis. In some frames, citrate-stabilized Au NC fiducial markers are visible on top of the DDQCs.

Supplementary Movie 8. Growth of the quasicrystal in the molecular dynamics simulation of the binary sphere model. Snapshots of this movie are shown in Figs. 4c-e (top) of the main text.